A Measurement of the Branching Fraction of the Decays of the tau- Lepton to 2pi- pi+ eta nu

by

Gregory James King
B.Sc., University of Victoria, 2004

A Thesis Submitted in Partial Fulfillment of the

Requirements for the Degree of
MASTER OF SCIENCE
in the Department of Physics and Astronomy

A Measurement of the Branching Fraction of the Decays of the tau- Lepton to 2pi- pi+ eta nu

by

Gregory James King
B.Sc., University of Victoria, 2004

Supervisory Committee

Dr. R. J. Sobie, Supervisor (Department of Physics and Astronomy)

Dr. J. M. Roney, Member (Department of Physics and Astronomy)

Dr. R. K. Keeler, Member (Department of Physics and Astronomy)

Dr. R. Tafirout, External Examiner (TRIUMF)

Supervisory Committee

Dr. R. J. Sobie, Supervisor (Department of Physics and Astronomy)

Dr. J. M. Roney, Member (Department of Physics and Astronomy)

Dr. R. K. Keeler, Member (Department of Physics and Astronomy)

Dr. R. Tafirout, External Examiner (TRIUMF)

Abstract

We investigate the decay mode $\tau^- \to \pi^-\pi^+\pi^-\eta\nu_\tau$, where the η subsequently decays to $\pi^+\pi^-\pi^0$ using $232\,\mathrm{fb}^{-1}$ data acquired by the *BABAR* detector. The branching fraction of $\tau^- \to \pi^-\pi^+\pi^-\eta\nu_\tau$ is found to be $(1.88 \pm 0.14 \pm 0.11) \times 10^{-4}$. The first error on the is measurement is purely statistical and the second error is estimated systematic error. This measurement is consistent with the prior experimental mesaurements at CLEO and *BABAR*.

Table of Contents

List of Tables

List of Figures

Acknowledgements

I wish to thank my supervisor, Dr. Sobie.

Dedications

This thesis is dedicated to Melina Young and my son Owen.

Chapter 1

Introduction

The large data sample of τ pair events collected by the *BABAR* Collaboration allows for detailed studies of rare τ lepton decays. Such rare decay modes are often poorly understood and require detailed experimental measurements to improve our understanding of the decay mechanisms. This work examines the $\tau^- \to \pi^-\pi^+\pi^-\eta\nu_\tau$ decay using the sub-decay $\eta \to \pi^+\pi^-\pi^0$.[1] This thesis presents a measurement of the branching fraction of the $\tau^- \to \pi^-\pi^+\pi^-\eta\nu_\tau$.

The τ pair events are produced at the PEP-II storage ring at the Stanford Linear Accelerator (SLAC). The primary physics goal of the *BABAR* experiment is the study of *CP*-violating asymmetries in the decay of neutral B mesons to CP eigenstates [2,3]. Also relevant to this work is the large sample of τ pair events that can be used to study the decay of the τ-lepton.

The objective is to search for $\tau^- \to \pi^-\pi^+\pi^-\eta\nu_\tau$ decays where $\eta \to \pi^+\pi^-\pi^0$, by selecting events with $(3\pi^-2\pi^+\pi^0)$ in the final state. The $\eta \to \pi^+\pi^-\pi^0$ decay is identified by requiring that the invariant mass of the $(\pi^+\pi^-\pi^0)$ system be close to the η mass ($m_\eta = 547\,\mathrm{MeV}$ [1]). We fit the $(\pi^+\pi^-\pi^0)$ mass spectrum to find the number of observed η candidates in order to obtain the branching fraction, $\mathcal{B}(\tau^- \to \pi^-\pi^+\pi^-\eta\nu_\tau)$.

[1] Charge conjugation is assumed throughout this thesis.

The Standard Model is discussed in chapter 2. A brief summary of the *BABAR* detector is presented in chapter 3. Event selection criteria is covered in Chapter 4. In Chapter 5, the results for the $\tau^- \to \pi^-\pi^+\pi^-\eta\nu_\tau$ branching fraction are detailed.

Chapter 2

Theory

This chapter begins with a short summary of the Standard Model (SM) and introduces particles which are constituents of the SM. The properties of the leptons and the quarks are introduced and an overview of the τ lepton is presented. Finally, a discussion of important observables in the SM is presented.

2.1 Standard Model

The fundamental concepts of classical physics involve particles and fields and modern physics unites these concepts in an attempt to describe the universe. Quantizing any classical field leads to a synthesis among the concepts of particles and fields; with the quanta of the fields being made up of particles with specific properties (e.g., spin, charge, mass). For example, the interaction between electrically charged particles is mediated by an exchange of photons. The description of the interaction dynamics between elementary particles and the three of the four fundamental forces observed in nature is known as the Standard Model (see, for example [4, 5]). The four fundamental forces in nature are: strong (or color dynamics); electromagnetic (or charge dynamics); weak (or flavor dynamics); and gravity (or geometry dynamics). Further, the electromagnetic and weak interactions can be unified into a 'single' interaction

which is called the *electroweak* force. Of the four forces in nature, the Standard Model provides a description of the strong, the weak and the electromagnetic forces (the force of gravity is assumed to be 'too weak to play a significant role in elementary particle physics' (for example, see [4, 6])). Each interaction is distinguished by its inherent strength and associated charge, as well as by its own particular set of conservation laws and selection rules.

The goal of particle physics is to identify the basic units of matter and the basic forces. It is expected that the smallest units of matter will interact in the simplest ways and that there will be a deep connection between basic units of matter and the basic forces [6].

Based on current experimental evidence, an elementary particle is an intrinsic building block of matter with no inherent structure. Such particles are usually categorized into three distinct group called: leptons, quarks, and mediators. According to the Standard Model, all 'matter' is built from a number of fundamental spin-$\frac{1}{2}$ particles (fermions): quarks and leptons. There are six leptons, and similarly, there are six 'flavours' of quarks[1]. Mediators, on the other hand, are responsible for the interactions between charged particles.

Table 2.1 and 2.2 list the fundamental leptons and quarks. Unlike leptons, quarks are confined to composite systems known as hadrons. Quarks carry an additional charge known as colour. However, unlike electric charge, colour charge comes in three kinds. The strong interaction is associated with the colour charge.

The known fundamental forces are mediated by a set of spin-1 vector particles (bosons). The photon is the associated mediator of the electromagnetic interaction. The weak force has three associated vector bosons, the $W^{\pm}$ and Z^0. On the other hand, the strong interaction is mediated by the gluon, and in the Standard Model

[1]There are also six anti-quarks and also six anti-leptons

lepton	charge	mass
ν_e	0	$< 2\,\mathrm{eV}\ /c^2$
e	-1	$0.511\,\mathrm{MeV}/c^2$
ν_μ	0	$< 0.19\,\mathrm{MeV}/c^2$
μ	-1	$105\,\mathrm{MeV}/c^2$
ν_τ	0	$< 18.2\,\mathrm{MeV}/c^2$
τ	-1	$1.777\,\mathrm{GeV}/c^2$

Table 2.1: Lepton electromagnetic classification. The particles are grouped according to generation, in order of increasing mass with respect to charged lepton of the associated generation.

quark	charge	mass
d	$-1/3$	3-7 MeV/c^2
u	$+2/3$	1.5-3.0 MeV/c^2
s	$-1/3$	$(95 \pm 25)\,\mathrm{MeV}/c^2$
c	$+2/3$	$(1.25 \pm 0.09)\,\mathrm{GeV}/c^2$
b	$-1/3$	$4.20 \pm 0.07\,\mathrm{GeV}/c^2$
t	$+2/3$	$174.2 \pm 3.3\,\mathrm{GeV}/c^2$

Table 2.2: Quark electromagnetic classification. The particles are grouped according to generation.

there are eight of them. Gluons also carry colour.

Mediator	Charge	Mass	Interaction
gluons	0	0	strong
photon (γ)	0	0	electromagnetic
$W^\pm$	± 1	$80.383 \pm 0.035\,\mathrm{GeV}/c^2$	weak
Z^0	0	$91.1876 \pm 0.0021\,\mathrm{GeV}/c^2$	weak

Table 2.3: Mediators of the three forces.

The Standard Model relies upon the machinery of quantum field theory to explain fundamental particles and interactions. Although each force relies upon underlying quantum field theory, most physical processes are represented by Feynman diagrams.[2]

[2]These diagrams represent an element of the Dyson expansion and only make sense in the weak

2.1.1 Electroweak Theory

Hadrons and leptons experience the weak interaction and may undergo weak decays. Such decays are often masked by strong and electromagnetic decays. It is only in the situation where the strong and electromagnetic interactions are suppressed that the weak modes may dominate.

Originally, the weak current interaction was regarded simply as a way to explain the phenomenon of weak decays. It did not constitute a proper theory. The only known way to convert the phenomenological description into a renormalizable theory required the introduction of spontaneously broken gauge symmetries to generate the masses of gauge bosons associated with weak interactions. The fundamental weak interaction Feynman diagrams are shown in figure 2.1. The $W^{\pm}$ boson can interact with a charged lepton and its associated neutrino, as well as with an up-type quark and a down-type quark. The neutral current and the associated Z^0 exchange involves couplings with almost all standard model particles, except the eight gluon.

Initially the electromagnetic and weak interactions look very different, but it is possible to unify the description with electroweak theory (see [5, 7]).

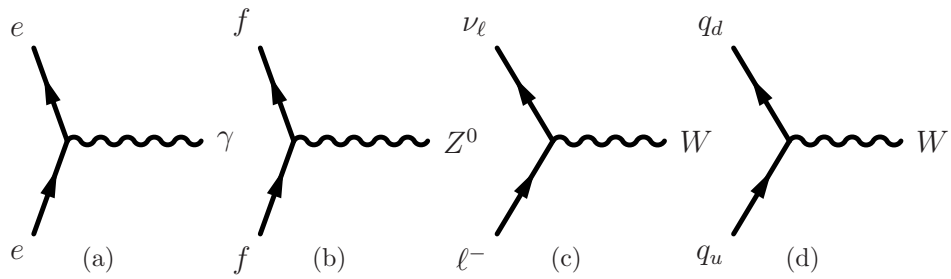

Figure 2.1: Example of tree level Feynman diagrams for interaction invovling matter and electroweak bosons, where $l \in \{e, \mu, \tau\}$.

'coupling' regime.

2.2 The τ lepton

The τ lepton was discovered more than 20 years ago by M. Perl *et al.* [8]. It provides a fascinating tool for testing a wide range of phenomena in the Standard Model from resonance physics to perturbative short distance physics. Moreover, because the τ is the only known lepton massive ($m_\tau \approx 1.777\,\mathrm{GeV}/c^2$) enough to decay into hadrons, its semi-leptonic decays are ideal for studying strong interaction effects. The τ lepton production mechanism at *BABAR* is shown in figure 2.2.

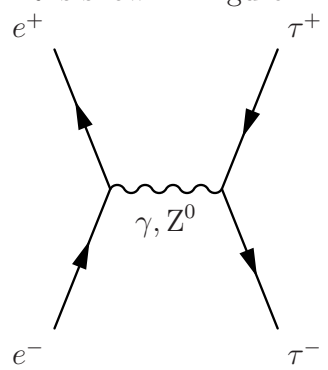

Figure 2.2: Electromagnetic τ pair production

The τ decay modes are categorised as either leptonic (see figure 2.3) or semi-leptonic (these decays include at least one hadron) decays (see figure 2.4). Decays of the τ lepton to hadrons exhibit a complex structure of resonances. Any description of τ decays should improve the understanding of the decay of such resonances including the final hadronic decay products (π, η, etc.). This structure also allows for the study of meson dynamics.

Because non-strange hadronic branching fractions represent the largest part of τ decays and since physics goals require measurements with small uncertainties, the study of six-pion decays can be used to test the CVC hypothesis[3] and isospin predictions (see [9,10]). Further, with a better understanding of the resonance substructure

[3]The CVC hypothesis can be tested by any τ decay which decays to an even number of pions.

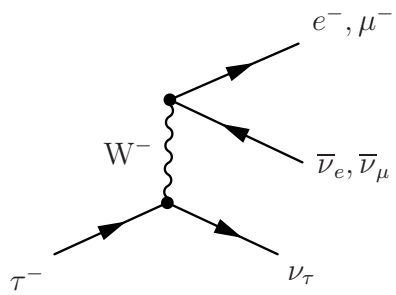

Figure 2.3: τ^- which decays into its associated neutrino (ν_τ) and either e^- and $\overline{\nu}_e$, or, μ^- and $\overline{\nu}_\mu$

in multi-hadronic decays, the hadronic backgrounds can be suppressed so that limits in the ability to directly measure the τ neutrino mass will be reduced.

For all hadronic channels, the τ decays proceeds through a two-body reaction into a ν_τ and a hadronic resonance, which subsequently decays into other mesons (see figure 2.4). This is commonly described as $\tau^- \rightarrow (\text{hadronic})^- \nu_\tau$, where the 4-momentum of the hadronic state is the sum of the final-state particles. In the rest frame of the decaying τ the energy of the hadronic system is completely determined by energy and momentum conservation. The matrix element for any semi-leptonic τ decay is complicated by hadronization.

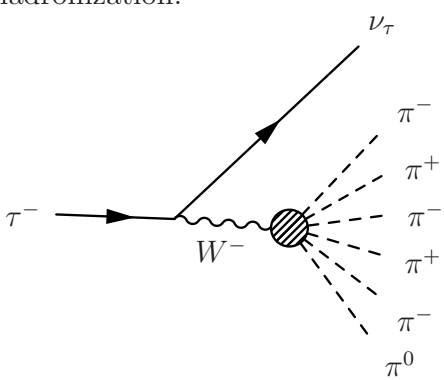

Figure 2.4: τ decay with all hadronization and resonance effects being represented by the shaded circle.

2.3 Decay Rate and Branching Ratio

The decay rate, Γ, represents the probability, per unit time, of a particle decaying. The mean lifetime is simply the reciprocal of the decay rate ($1/\Gamma$). However, most particles can decay through several channels. In such cases, we define the total decay rate as the sum of the individual decay rates:

$$\Gamma = \sum_{i=1}^{n} \Gamma_i \tag{2.1}$$

The lifetime of such a particle is the reciprocal of Γ_{tot}.

Branching ratio is defined as the fraction of all particles of the given type that decay through a specific decay mode. Branching ratios are determined by the decay rates:

$$\mathcal{B}(i^{\text{th}}\ \textit{decay mode}) = \frac{\Gamma_i}{\Gamma} \tag{2.2}$$

2.3.1 Fermi's Golden Rule

Fermi's Golden Rule provides a prescription for combining dynamical and kinematical information to obtain observable quantities such as decay rates and scattering cross sections. The transition rate for an arbitary process is determined by the matrix element and the phase space according to:

$$\text{transition rate} = 2\pi|\mathcal{M}|^2 \mathrm{d}R \tag{2.3}$$

The matrix element ($\mathcal{M}$) contains the dynamical information. On the other hand, $\mathrm{d}R$, the phase space factor, contains only kinematical information and it depends on masses, energies, and momenta of the initial and final state particles. The larger the available phase space the more likely a transition is to occur.

Suppose a particle, p_1, decays into several other particles, $(p_2, p_3, ..., p_n)$, then the

transition rate is described by the Golden Rule for Decays:

$$\mathrm{d}\Gamma = \frac{S|\mathcal{M}_{p_1 \to p_2 + \ldots + p_n}|^2}{2m_1} \times \mathrm{d}R_n \tag{2.4}$$

where S is a statistical factor correcting for identical particles in the final state, and $\mathrm{d}R_n$ is the associated n particle phase space factor.

2.4 Resonances

A resonance is a short-lived state with a mass, a lifetime, and a spin (other quantum numbers may be used to characterize the state, including angular momentum, parity, etc.). Frequently a resonance is identified with a very short-lived particle or bound state that cannot be directly observed by a detector. Since a resonance has an associated lifetime, it is expected that its characteristic mass will have an associated width. Because many subatomic particles' lifetimes are too short to be observed directly, the existence of these particles is usually inferred from a peak found in the mass distribution of decay products. Resonances are commonly observed in τ lepton decays which involve hadrons. For example, in the decay $\tau^- \to \pi^-\pi^+\pi^-\eta\nu_\tau$, the η meson's lifetime is too short for direct observation, it can only be inferred by an examination of it's decay products.

The decay rate is measured by using the energy dependence of cross section given by the Breit-Wigner cross section formula (see [1]):

$$\sigma(E) \approx B_{in} B_{out} f_{BW}(E; M_0, \Gamma); \tag{2.5}$$

$$f_{BW}(E; M_0, \Gamma) = \frac{4\pi}{k^2}\left[\frac{\Gamma^2/4}{(E - m_0)^2 + \Gamma^2/4}\right],^{4} \tag{2.6}$$

[4]The relativistic Breit-Wigner is given by:

$$\frac{12\pi}{m_0^2}\Gamma_{\mathrm{in}}\Gamma_{\mathrm{out}}\frac{s}{(s-m_0^2)^2+\frac{s^2}{m_0^2}\Gamma^2}$$

where Γ is the width, $\sigma(E)$ is the cross section of the process at energy E, m_0 is the mean mass of the particle, B_{in}/B_{out} is the branching fraction for the resonance into the initial/final-state channel.

2.4.1 Semi-leptonic τ Decay Width

For a semi-leptonic of the τ, the matrix element is (ignoring the propagator of the $W^{\pm}$ boson):

$$\mathcal{M} \propto J^{\mu}_{\text{lep}} J^{\text{had}}_{\mu} \tag{2.7}$$

where, J^{μ}_{type} is the vector-current associated with weak leptonic or hadronic interactions. The definition of leptonic current can be found in [4, 5].

We do not know how the $W^{\pm}$ and Z^0 couple with composite structures like hadrons. The term J^{had}_{μ} (also known as the hadronic form factor) is not known *a priori*[5]. The hadronic form factor has to be determined by experiment.

In the situation where hadronization produces a single pion ($\tau^- \to \pi^- \nu_\tau$) the hadronic current can be reduced to $J^{\text{had}}_{\mu} = f_\pi p_\mu$ (see, for example, [5, 11]), where p_μ is the four-momentum of the π^- and f_π is known as the pion decay constant. The pion decay constant can be obtained by measuring the π^- lifetime. For example, the partial decay width for the reaction is

$$\Gamma(\tau^- \to \pi^- \nu_\tau) = \frac{G_{\text{F}}^2 f_\pi^2 \cos^2(\theta_{\text{C}}) m_\tau^3}{8\pi} \left(1 - \frac{m_{\pi^-}^2}{m_\tau^2}\right)^2, \tag{2.8}$$

where G_{F} is the Fermi coupling constant, θ_{C} is the Cabibbo angle.

[5]Technically, the virtual $W^{\pm}$, which is responsible for the decay of the τ lepton actually couples to the free quarks. However, at energies below $\mathrm{m}_\tau c^2$ quarks are strongly bound into mesons. Decays of the τ lepton can be described by a hadronic current coupling to the $W^{\pm}$. This hadronic current comes from the vacuum and leads to a final state with one or more mesons. This is why the term is called the hadronic current rather than quark current.

2.5 Experimental Branching Fraction

The general experimental equation used to determine the branching fraction of a particular decay is:

$$\mathcal{B}(\tau^{\pm} \to \mathrm{X}^{\pm}\nu_{\tau}) = \frac{\mathrm{N_{sel}}}{2\mathrm{N}_{\tau^+\tau^-}} \tag{2.9}$$

where $\mathrm{N_{sel}}$ is the number of events found and $\mathrm{N}_{\tau^+\tau^-}$ is the number of τ pair events. Since this is an experimental measurement, the equation must be modified in order to include experimental efficiency and remove background contamination. This leads to:

$$\mathcal{B}(\tau^{\pm} \to \mathrm{X}^{\pm}\nu_{\tau}) = \frac{\mathrm{N_{sel}}}{2\mathrm{N}_{\tau^+\tau^-}} \frac{1 - f_{\mathrm{bkg}}}{\epsilon_{\mathrm{sel}}} \tag{2.10}$$

where ϵ_{sel} is the efficiency for selecting $\tau^{\pm} \to \mathrm{X}^{\pm}\nu_{\tau}$, f_{bkg} is the estimate fraction of background contamination.

Chapter 3

BABAR Detector

This chapter is a detailed overview of the hardware and software used to acquire data sets at the *BABAR* detector. The linear accelerator and PEP-II storage rings are discussed. An outline of the *BABAR* detector's architecture with a primary focus on the components used for detecting final state particles is presented.

3.1 Introduction

Progress in experimental physics is linked with improved methods of measurement. In high energy physics, scientists use particle accelerators and detectors as their primary experimental tools. Accelerators impart high energies to charged particles (both sub-atomic and atomic), which then collide with targets of various kinds such as charged particles and atoms. Often, the higher the energy of an accelerated particle, the better it will serve to test properties of fundamental interactions and fundamental particles[1]. The presence and behaviour of the particles emerging from these collisions are recorded by detectors near or surrounding the interaction point in order to reconstruct information about the interaction.

The charged and stable constituents of ordinary matter - electrons and protons -

[1]This *rule* is not always true. The *BABAR* detector provides precision measurements related to b-quarks and τ leptons without the highest available beam energies.

are easy to produce in isolation. There are two common ways of 'producing' electrons: by using a laser to knock them off the surface of a semiconductor, or by heating up a piece of metal until electrons come flying off. Utilizing a positively charged plate with a small hole in it, the electrons passing through the hole can be considered a 'beam'[2]. More exotic particles come from three main sources: cosmic rays, nuclear reactors, and particle accelerators.

The production of massive particles requires higher energy collisions. High 'centre of mass energy' conditions are easier to achieve by colliding two high-speed particles head-on rather than firing one particle at a stationary target. Thus, most high energy physics experiments involve colliding beams from intersecting storage rings.

A high energy e^+e^- collision can give rise to a shower of particles, that spreads outward from an interaction point. Results are read from an array of specialized subdetectors, each designed to measure some of the properties of these particles.

At energies above 10 MeV, photons interact primarily through the creation of an electron-positron pairs. Electrons or positrons resulting from this interaction can be detected similarly to other charged particles. Neutrinos can only be detected by observing their weak interactions with nuclei or with electrons[3]. Neutron and other neutral hadron detection relies upon observing the strong interactions with nuclei and the subsequent emission of charged particles or photons. Charged particles can be detected directly through their electromagnetic interactions. When a charged particle traverses a layer of detector material, three processes can occur: atoms can be ionized; the particle can emit Cherenkov radiation; or, the particles can cause the emission of transition radiation.

Most detectors follow a standard design geometry. Moving from the interaction

[2]This device is known as an *electron gun*.

[3]Neutrino detection probability is very low. However, the presence of a neutrino can be inferred from the missing energy in an event.

point outwards a high energy physics detector incorporates the following devices:

1. Tracking Chamber;
2. Calorimetry;
3. μ detectors;

A tracking chamber provides momentum measurement of the charged particles leaving the interaction point. Energy measurements of photons and charged particles are provided by calorimetry. Finally, muon identification detectors attempt to determine whether a charged track was produced by a muon rather than a pion, a kaon or a proton.

3.2 The Stanford Linear Accelerator Center

The Stanford Linear Accelerator Center (SLAC), which became operational in 1966 is 3.2 km in length, and is the longest linear accelerator in the world (see Figure 3.1). A linear accelerator or linac uses electromagnetic waves to accelerate charged particles to near the speed of light. Electrons are knocked off the surface of a semiconductor using a laser, while positrons are created by firing an electron beam at a tungsten target.

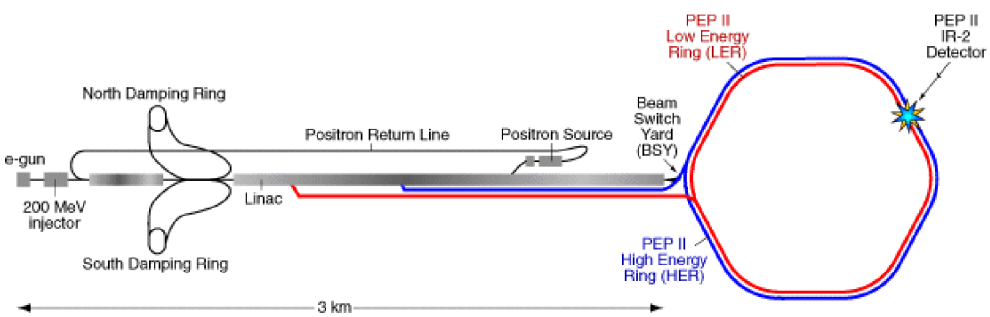

Figure 3.1: SLAC and PEP-II Rings Schematic [12].

After traveling about three metres down the linear accelerator, electron and positron bunches achieve an energy on the order of 10 MeV. However, these 'bunches' have a tendency to disperse in the plane perpendicular to their travel. To counteract this dispersion, the electron and the positron bunches are fed into damping rings. As these bunches circulate in the damping ring, they lose energy by synchrotron radiation, but are re-accelerated each time they pass through a cavity fed with electric and magnetic fields. The synchrotron radiation decreases the motion in all directions and damps out motion in the perpendicular plane, while the re-accelerating kicks keep the particles moving at relativistic speeds. The bunches are then re-injected into the linear accelerator.

Both electrons and positrons are accelerated down a long copper tube as they are propelled to relativistic speeds via microwaves supplied by a series of klystrons. After traveling the length of the accelerator, the particles are fed into the PEP-II (Positron-Electron Project-II) storage rings. One of the PEP-II rings stores high energy electrons (9 GeV). A second ring (above the electron ring) stores lower energy positrons (3.1 GeV). The configuration of the rings makes it possible to use asymmetric beam energies for the study of CP violations of the B meson. The beams collide near the centre of the BaBar detector. The PEP-II rings were designed to provide high luminosity for B and τ physics of $\mathcal{O}(10^{34})$ cm^{-2}s^{-1}.

The PEP-II storage ring system is designed to operate with a center of mass energy of 10.58 GeV, corresponding to the mass of the Υ(4s) resonance. While most of the data are recorded at the peak of the Υ(4s) resonance, about 12% are taken at a center of mass energy 40 MeV lower to allow for studies of the non-resonant background.

3.3 The *BABAR* Detector

The *BABAR* detector is specifically designed to handle the asymmetric beam energies provided by the PEP-II storage rings. It is offset relative to the interaction point by 0.37 m in the direction of the lower energy beam. The right-handed coordinate system is anchored on the main tracking system with the z-axis coinciding with its principle axis or the direction of the e^- beam. The positive y-axis points upwards and the positive x-axis points away from the center of the PEP-II storage rings. The most important requirements for B and τ physics are summarized below;

- a large uniform acceptance down to small polar angles relative to the boost direction;
- excellent reconstruction efficiency for charged particles down to 60 MeV/c and for photons to 20 MeV;
- very good momentum resolution;
- excellent energy and angular resolution for the detection of photons with energy 20 MeV to 4 GeV; and
- very good vertex resolution, transverse and parallel to the beam direction.
- efficient electron, muon, and hadron identification; and

The *BABAR* detector meets these requirements using several independent detector elements. The inner detector consists of a silicon vertex tracker (SVT); a drift chamber (DCH); a ring-imaging Cherenkov detector (DIRC); and a CsI calorimeter (EMC). These detector subsystems are surrounded by a 1.5 T superconducting solenoid. The steel flux return (IFR) is instrumented for muon and neutral hadron detection. The schematics of the *BABAR* detector are shown in Figure 3.2 and 3.3.

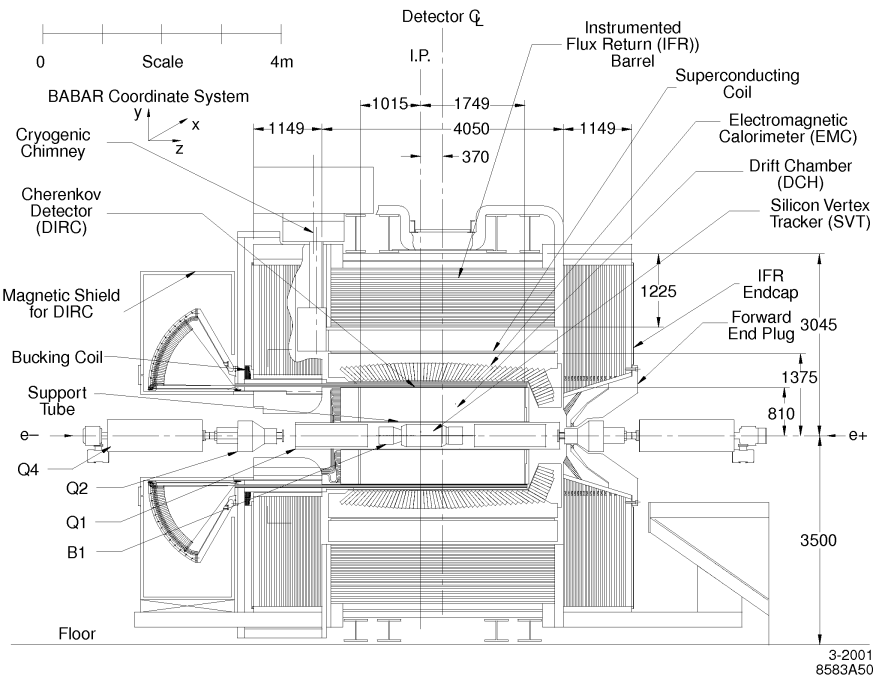

Figure 3.2: *BABAR* detector longitudinal section

3.3.1 Particle Tracking

The charged particle tracking system has two components: a silicon vertex tracker (SVT) and a drift chamber (DCH). The SVT provides position and angle information for the measurement of the vertex position just outside the interaction region. The DCH's principal purpose is the detection of charged particles and the measurement of their momenta and angles. The magnet supplies a high magnetic field (1.5 T) along the axis of the beam pipe, which bends the path of charged particles in the detector and allows for the determination of a particle's momentum.

3.3.2 Silicon Vertex Tracker

The SVT was designed to provide precise reconstruction of charged particle trajectories and decay vertices near the interaction region, it is composed of five layers of

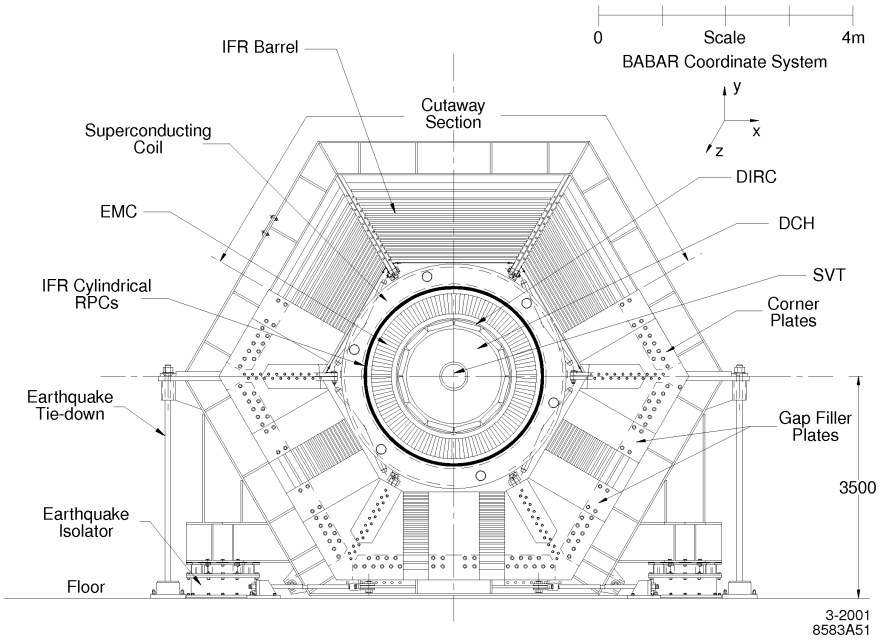

Figure 3.3: *BABAR* detector end view.

double-sided silicon strip detectors centered on the beam pipe. Theses five layers are organized in 6, 6, 6, 16, and 18 modules respectively (see Figures 3.4,3.5). The ϕ measuring strips run parallel to the beam, while the z measuring strips are oriented transversely to the beam axis. The inner three module layers are straight, with the innermost layer positioned at a radius of 32 mm from the beam axis, while the modules of layers 4 and 5 are arch-shaped.

The SVT provides stand-alone tracking for particles with low transverse momentum near the interaction point. Finally, double-sided sensors provide up to ten measurements of dE/dx per track. With 10 dE/dx measurements, a 2σ separation between kaons and pions can be achieved up to a momentum of 500 MeV/c.

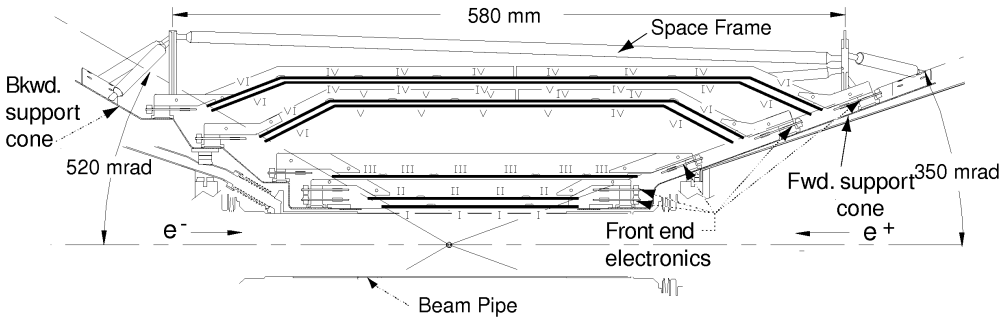

Figure 3.4: Schematic View of SVT: longitudinal section. The roman numerals label the six different types of sensors. The arch design was chosen to minimize the amount of silicon required to cover the solid angle, while increasing the crossing angle for particles near the edges of acceptance.

3.3.3 Drift Chamber

The primary purpose of the DCH is the momentum measurement of charged particles. DCH measurements provide an extra set of constraints on the impact parameter from the SVT and the direction of charged tracks near the interaction point. If a particle decays outside the SVT, the reconstruction relies solely on the DCH. The DCH also provides a mechanism for particle identification of particles by measuring the ionization loss (dE/dx).

The DCH is designed to track particles with transverse momentum greater than 180 MeV/c. The tracker is a 2.80m long cylinder with an outer radius of .809m, and an inner radius of .236m, and encloses the SVT and beam pipe (see Figure 3.6 for a schematic of the DCH).

The DCH contains 7104 hexagonal drift cells arranged in 10 super layers, of 4 layers each (see Figure 3.7). The chamber is pressurized with a (4:1) helium - isobutane gas mixture. The electric field lines lie in the $r - \phi$ plane perpendicular to the axial magnetic field. This field is generated by an arrangement of potential wires

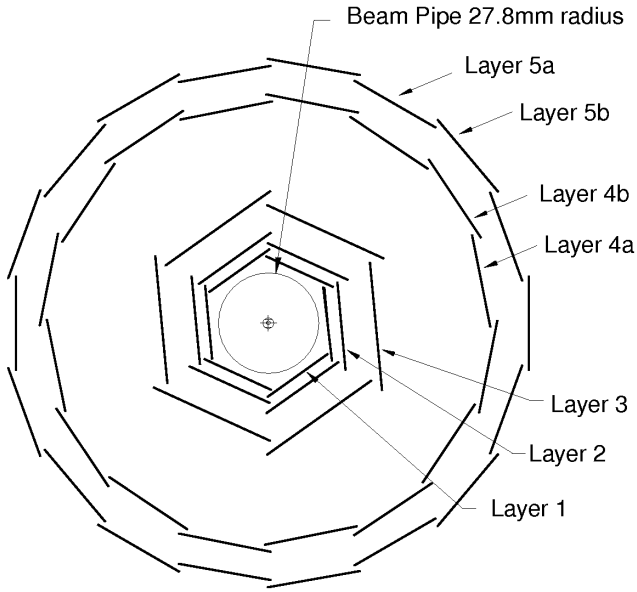

Figure 3.5: Schematic View of SVT: transverse section.

which are parallel to each other and surround the signal (anode) wire in the center of the cell. Roughly half of the signal wires are parallel to the **B**-field, while others are skewed and run at various stereo angles relative to this axis. This enables the reconstruction of the z position of the track with limited precision. By choosing low-mass wires and using a helium-based gas mixture, the multiple scattering inside the DCH is minimized[4]. When a charged particle enters the drift chamber, it ionizes the gas. The resulting ionization is detected by the sense wires that run the entire length of the detector. Further, as the particle travels outward, measurements of energy loss by ionization are taken (dE/dx). The DCH measures dE/dx with a resolution 7.5% and allows for π/K separation up to 700 MeV/c.

[4]If the momentum of the charged particle is less than 1 GeV/c, multiple scattering is a significant, and can be the dominant limitation on the track parameter resolution.

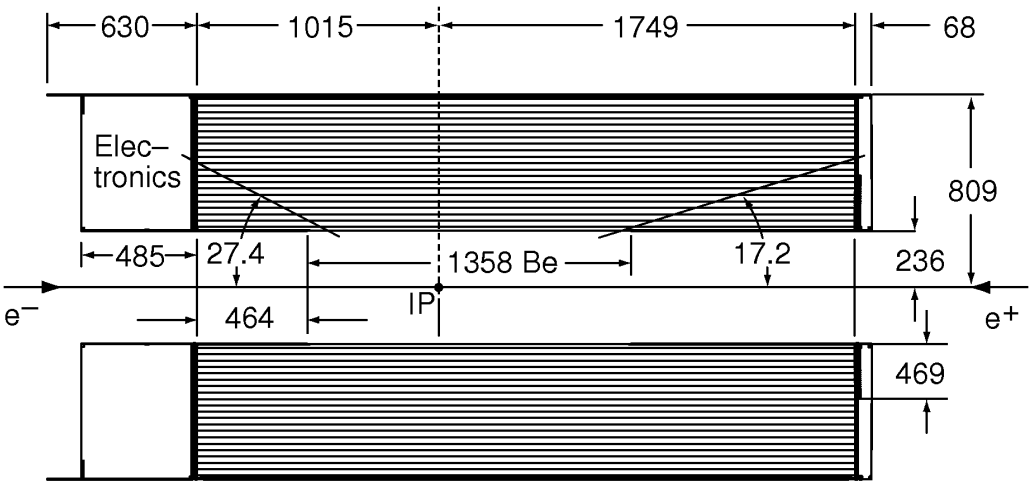

Figure 3.6: Longitudinal section of the DCH with principal dimensions.

3.3.4 Superconducting Solenoid

The *BABAR* magnet system consists of a superconducting solenoid, a segmented flux return and a field compensating coil. Momentum measurement in the tracking chambers is made possible by the superconducting solenoid. A solenoid magnetic field of 1.5 T achieves the needed momentum resolution for charged particles.

3.3.5 Track Reconstruction

Charged tracks are defined by five parameters, $(\mathrm{d}_0, \phi_0, \omega, \mathrm{z}_0, \tan(\lambda))$ with their associated error matrices. These parameters are measured at the point of closest approach to the z-axis; d_0 and z_0 are the distance of this point from the origin of the coordinate systems in the x-y plane and along the z-axis respectively. λ is the dip angle relative to the transverse plane. The angle ϕ_0 is the azimuth of the track and $\omega = 1/\mathrm{p}_\mathrm{t}$ is the track curvature. The track-finding and fitting procedures take into account the distribution of material in the detector and the map of the magnetic field.

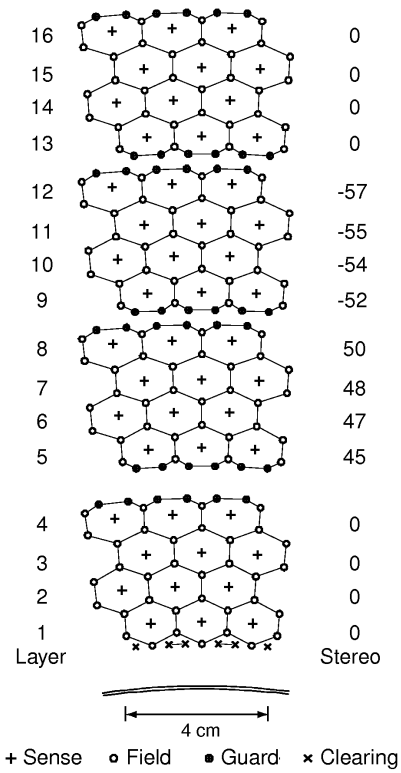

Figure 3.7: Schematic layout of drift cells for the four innermost superlayers. Note that lines have been added between field wires to aid in visualization of cell boundaries. The numbers on the right side are the stereo angle of sense wires in mrad.

The transverse momentum resolution is found to be:

$$\frac{\sigma_{p_t}}{p_t} = 0.13 \pm 0.01\% \cdot p_t + (0.45 \pm 0.03)\% \tag{3.1}$$

where the transverse momentum p_t is measured in GeV/c.

3.3.6 Electromagnetic Calorimeter

The interaction of photons and electrons in matter at energies well above 10 MeV is dominated by pair creation and Bremsstrahlung, respectively. An alternating sequence of interactions of these types leads to a cascade or 'shower' of electrons,

positrons and photons (see Figure 3.8). As particle energies become smaller other processes such as ionization and Compton scattering also become important.

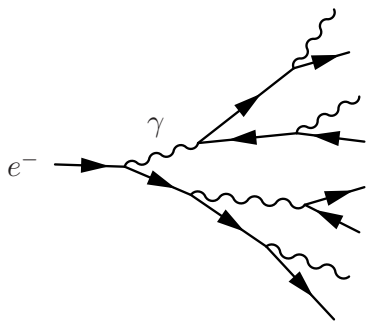

Figure 3.8: Diagram of an Electromagnetic Cascade.

The electromagnetic calorimeter (EMC) is designed to measure electromagnetic showers over the energy range from 20 MeV to 9 GeV. It offers excellent efficiency, as well as very good energy and angular resolution.

The EMC is a hermetic, total-absorption calorimeter, composed of a finely segmented array of thallium-doped cesium iodide (CsI(Tl)) crystals. The intrinsic efficiency for detection of photons in a CsI(Tl) Calorimeter is close to 100% above 20 MeV. The read-out of the crystals is done with silicon photodiodes. The EMC consists of a cylindrical barrel, with an end cap in the forward direction. Ninety percent coverage of the solid angle is provided in the center mass system, with $(15.8° - 141.8°)$ coverage in the polar angle and full coverage in the azimuthal angle. The barrel of the EMC is lined with 5760 trapezoidal CsI(Tl) crystals, which are arranged in 48 polar-angle rows. The crystals are oriented such that they point towards the interaction point (IP). Crystals increase in length from (16-17)X_0[5] in steps of $0.5X_0$ every 7 crystals for $\cos(\theta) = 0 \rightarrow 1$. The forward end cap contains 820 crystals, and spans a

[5] X_0 is known as the radiation length of the material. Radiation length is both (a) the mean distance over which a high-nergy electron lose all but $1/e$ of its energy by bremsstrahlung and (b) 7/9 of the mean free path for pair production by a high-energy photon [1].

solid angle corresponding to $0.893 \leq \cos(\theta) \leq 0.962$ in the laboratory frame.

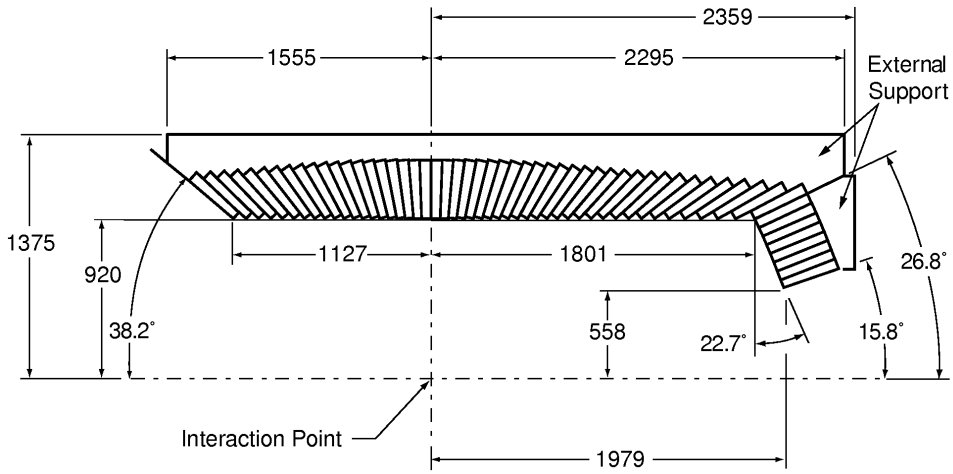

Figure 3.9: A longitudinal cross section of the top half of the EMC. Notice that the detector is axially symmetrical around the z-axis. All dimensions are in mm.

The energy resolution of a homogeneous crystal calorimeter is given by the empirical equation [2]:

$$\frac{\sigma_E}{E} = \frac{a}{\sqrt[4]{E(\,\mathrm{GeV})}} \oplus b \tag{3.2}$$

where E and σ_E refer to the energy of a photon and its rms error, measured in GeV. Further, the $\oplus$ means that the terms are added in quadrature. The angular resolution is determined by the transverse crystal size and the distance from the interaction point. It can be parametrized as a sum of energy dependent and a constant terms [2],

$$\sigma_\theta = \sigma_\phi = \frac{d}{\sqrt{E(\,\mathrm{GeV})}} + e \tag{3.3}$$

where the energy E is measured in GeV.

A typical electromagnetic shower spreads over many adjacent crystals, forming a cluster of energy deposits. Pattern recognition is used to distinguish between single clusters with one energy maximum and merged clusters with more than one 'local'

Parameter	Fit Value(%)	Error (%)
a	2.32	0.30
b	1.85	0.12
Parameter	Fit Value(mrad)	Error (mrad)
d	3.87	0.07
e	0.00	0.04

Table 3.1: EMC Energy and angular resolution parameters.

energy maximum (an energy maximum is commonly referred to as a bump). The algorithms also determine whether a bump is associated with a charged or neutral particle.

Electrons are separated from charged hadrons almost exclusively on the basis of the energy measurements from the EMC and the momentum measurements in the DCH. In addition, the dE/dx energy loss and Cherenkov angle are required to be consistent with an electron. The important variable for discrimination of hadrons from electrons is the ratio of shower energy to the track momentum (E/p).

3.3.7 DIRC and IFR

One manifestation of the electromagnetic interaction of charged particles in matter is Cherenkov radiation. When a charged particle's velocity exceeds that of light in the transparent medium, electromagnetic radiation is emitted.

The DIRC is a device providing separation of pions and kaons from about 500 MeV/c to the kinematic limit of 4.5 GeV/c. The Cherenkov light generated in a rectangular quartz bar by charged particles propagates along the bar by total internal reflection, which preserves the angle of emission. The Cherenkov cone emerges from the end of the bar and is focused onto an array of photomultipliers. Images of the Cherenkov rings are reconstructed from the position and time of arrival of

the signals in the photomultiplier tubes. By measuring both the angle of emission of Cherenkov radiation and the momentum of the charged particle it is possible to reconstruct the particle's mass.

The steel flux return is also known as the instrumented flux return (IFR). The IFR is used to identify muons and detect neutral hadrons over a range of momenta and angles. The IFR uses the steel flux return of the magnet as a muon filter and hadron absorber. Single gap resistive plate chambers (RPCs) with two coordinate readouts are the detectors. The RPCs are installed in the gaps of the segmented steel of the barrel and end doors of the flux return. There are 19 RPC layers in the barrel and 18 in the endcaps. RPCs are also installed between the EMC and the magnet cryostat to detect any particles exiting the EMC. The IFR has large solid angle coverage, good efficiency, and high background rejection for low momentum muons (below 1 GeV/c).

3.3.8 Event Trigger

A trigger, in the context of particle detector, is a collection of devices providing a 'fast' signal whenever some interesting physics event has happened. A trigger is associated with at least one part of a detector. The trigger signal causes the detector information pertaining to these and other subdetectors to be conditionally[6] passed onto a higher level trigger system or to be recorded. In *BABAR*, an efficient and robust trigger system is critical for transmitting data that have a high probability of containing good physics events.

The *BABAR* trigger system operates as a sequence of two independent stages. The second stage is conditional upon the first. The first stage is the Level 1 (L1) trigger and the second stage is the L3 software trigger. The L1 trigger is required to interpret

[6]These conditions are often called the event signature.

incoming detector signals, and recognize and remove beam-induced background[7]. The L1 trigger selection is based on data from DCH, EMC, and IFR. The L3 software trigger selects events of interest which are to be stored for later processing. The Level 3 (L3) trigger relies upon the complete event and L1 trigger information to make its decision. The L3 output rate is limited to 120 Hz.

The L1 trigger filters events based on charged tracks in the DCH, showers in the EMC, and hits in the IFR. The DCH and EMC triggers are primarily responsible for the identication of physics events in the detector, and the IFR trigger is responsible for rejecting events from cosmic rays and triggering on μ-pairs and neutral hadrons.

The L3 trigger reconstructs the events and classifies them according to their topology. The reconstructed quantities from the DCH and EMC are subjected to more stringent demands which reduce the amount of beam background and Bhabha contamination.

Event Type	Cross Section (nb)	Production Rate (Hz)	L1 Trigger Rate (Hz)
$b\bar{b}$	1.1	3.2	3.2
other $q\bar{q}$	3.4	10.2	10.1
$e^+ e^-$	53	159	156
$\mu^+ \mu^-$	1.2	3.5	3.2
$\tau^+ \tau^-$	0.9	2.8	2.4

Table 3.2: Cross Sections, productions and trigger rates for the principal physics processes at 10.58 GeV for luminosity of $3 \times 10^{33}\text{cm}^{-2}\text{s}^{-1}$. The $e^+ e^-$ cross section refers to events with either the e^+, e^-, or both inside the EMC detection volume. [2]

3.3.9 Event Reconstruction Chain

The reconstruction software uses the information from the various subdetectors and reconstructs them into the basic particle objects; tracks in the SVT and DCH and

[7]A small amount of common backgrounds, including beam-induced backgrounds, are accepted by the trigger for calibration and diagnostic data.

clusters in the EMC and IFR. Particle identification (PID) algorithms are used to assign probable identities to the particles. Event reconstruction takes place in a series of three steps by which candidates gain 'physical' properties (e.g. momentum, charge, energy, PID).

3.3.10 Simulation of the Detector

The aim of simulation production is to create a collection of Monte Carlo 'data' sets that mimic real data collection as closely as possible, in a theoretically consistent framework.[8]. It is not enough to generate the physical properties of a given decay. It is also vital to simulate the propagation of the particles through the various components of the detector and map possible interactions. Several stages of analysis are needed to produce these simulated data:

1. Generation of the underlying physics event;
2. Particle traversal and calculation of the idealized energy deposits in the detector;
3. Overlaying of backgrounds and digitization of the energy deposits; and
4. Reconstruction of the event.

The final step of the simulation is equivalent to that for real data being reconstructed. It takes collections of synthetic digital detector output and runs the full reconstruction chain, invoking reconstruction modules within the SVT, DCH, DRC, EMC and IFR sub-systems. The output collection is designed to be used in a physics analysis.

[8]Results are not changed because our detector response appears to be different than the simulated detector (differences in the real and theoretical detector are often an indication of new physics, or the sign of a failure in a detector component).

3.4 Detector Summary

The luminosity attained at PEP-II makes it possible to reach the sensitivities required to observe rare τ decay modes. As well, the capabilities of the *BABAR* detector allow measurements of common τ decay properties with a precision that rivals or exceeds prior experiments. Although the experiment is optimized for B physics, it is still well suited to perform τ physics. Most of the design choices for making a 'τ-factory' are similar to that of a 'B-factory'.

Chapter 4

Selection of $\tau^- \to \pi^-\pi^+\pi^-\eta\nu_\tau$

Physics involving τ leptons at *BABAR* follows a standard selection procedure. First, a loose pre-selection is used to identify τ pair events from the entire *BABAR* data collection. We require events to be classified as having one τ decaying to one charged particle and the other τ to at least three charged particles and are said to be in the 1-N topology. To minimize the background from hadronic, two-photon, and other di-lepton events, one of the τ leptons is required to decay into one of two leptonic modes, $\tau^- \to \mu^-\nu_\tau\overline{\nu}_\mu$ or $\tau^- \to e^-\nu_\tau\overline{\nu}_e$. In the other hemisphere we look for events which have properties that are consistent with $\tau^- \to 3\pi^-2\pi^+\pi^0\nu_\tau$.

4.1 Monte Carlo Samples

Monte Carlo events are used to determine backgrounds, selection efficiencies, and resolutions. Generic τ pairs production is simulated with the KK2F Monte Carlo event generator [13]. Each τ lepton decay is modeled with Tauola [13, 14].

Each Monte Carlo sample has been weighted in order to match the integrated luminosity of the data. The weights w_i is calculated as follows:

$$w_i = \frac{\sigma_i}{\mathrm{N}_i} \int \mathscr{L}_{\mathrm{data}} \mathrm{d}t \tag{4.1}$$

where $\int \mathscr{L}_{\text{data}} \mathrm{d}t$ is the integrated luminosity of the data sample, σ_i is the cross section for the producing the Monte Carlo sample i and N_i is the number of generated events for the ith sample.

Generic MC Sample	σ(nb)	N	Effective Luminosity (fb^{-1})
$\tau\tau$	0.919	1.90×10^8	207
uds	2.09	3.14×10^8	150
$c\bar{c}$	1.30	2.74×10^8	211
$B\overline{B}$	0.58	3.72×10^8	642
$B^0\overline{B}^0$	0.52	3.68×10^8	708

Table 4.1: The computed weights for each of the generic Monte Carlo samples. The $\tau\tau$ Monte Carlo sample does not include the $\tau^- \to 3\pi^- 2\pi^+ \pi^0 \nu_\tau$ channel.

In addition, special samples of $\tau^+\tau^-$ events were created using `EvtGen` [15]. These samples require that one τ lepton decays to a generic mode and the other τ decays into one of the following final states:

- $\tau^- \to \eta\pi^-\pi^+\pi^-\nu_\tau$
- $\tau^- \to \omega\pi^-\pi^+\pi^-\nu_\tau$

One of the samples is generated using $\tau^- \to \mathrm{f}_1(1285)\pi^-\nu_\tau \to \pi^-\pi^+\pi^-\eta\nu_\tau$ and another is generated without the intermediate $\mathrm{f}_1(1285)$ resonance, $\tau^- \to \pi^-\pi^+\pi^-\eta\nu_\tau$. The $\mathrm{f}_1(1285)$ meson decays included in the simulation are $\mathrm{f}_1(1285) \to \pi^+\pi^-\eta$ and $\mathrm{f}_1(1285) \to \pi \mathrm{a}_0(980) \to \pi^+\pi^-\eta$.

In addition to scaling the generic Monte Carlo to match the recorded integrated lumonisity of the data, we apply a veto to $\tau^- \to 3\pi^- 2\pi^+ \pi^0 \nu_\tau$ events that are simulated as a pure phase space decay. This veto does not affect the determination of the number of η's. Further, we scale the η signal Monte Carlo to correspond to the branching fraction determined by this measurement. The ω signal events are also scaled according to a branching fraction estimate of the mode $\tau^- \to \pi^-\pi^+\pi^-\omega\nu_\tau$.

Signal MC Sample	N_i
$\tau^- \to \pi^-\pi^+\pi^-\eta\nu_\tau$;	100,000
$\tau^- \to f_1(1285)\pi^-\nu_\tau \to \pi^-\pi^+\pi^-\eta\nu_\tau$;	100,000
$\tau^- \to f_1(1285)\pi^-\nu_\tau \to (\pi a_0(980))\pi^-\nu_\tau \to \pi^-\pi^+\pi^-\eta\nu_\tau$;	100,000
$\tau^- \to \omega\pi^-\pi^+\pi^-\nu_\tau$;	80,000

Table 4.2: Number of events in signal Monte Carlo samples. The Monte Carlo generator was configured so that 50% of the η mesons decay to π^+ π^- π^0 and the other 50% to $\gamma\gamma$.

4.2 Selection of τ Pair Events

The first step is the identification of $e^+e^- \to \tau^+\tau^-$ pairs. The background processes in e^+e^- collisions are shown in Figure 4.1, and include Bhabhas (Figures 4.1a,4.1b), dimuon (Figure 4.1b), $e^+e^- \to q\bar{q}$ (Figure 4.1b), and two-photon events (Figure 4.1c). τ pair events are usually characterized by two collimated back-to-back jets with low multiplicity and accompanied by missing energy and momentum due to neutrinos that escape detection.

One of the main background processes is from $e^+e^- \to q\bar{q}$ events where the quarks hadronize into many particles. The average multiplicity of hadrons increases with the centre-of-mass energy; this also increases the separation between τ and pure hadronic events at high energies. Typically, the number of hadrons produced is large ($\mathcal{O}(10)$), which commonly distinguishes these events from τ hadronic decays.

In *BABAR* the full data set is passed through various loose pre-selection criteria to select events with some set of desired properties. The pre-selection process is known as a 'skim' and is designed to ensure that the event was created by a 'true' e^+ e^- interaction and to select events based on specific physics signatures.

Our analysis starts with the *BABAR* Tau1N skim. The event is divided into two hemispheres based on the plane perpendicular to the thrust axis. We assign the

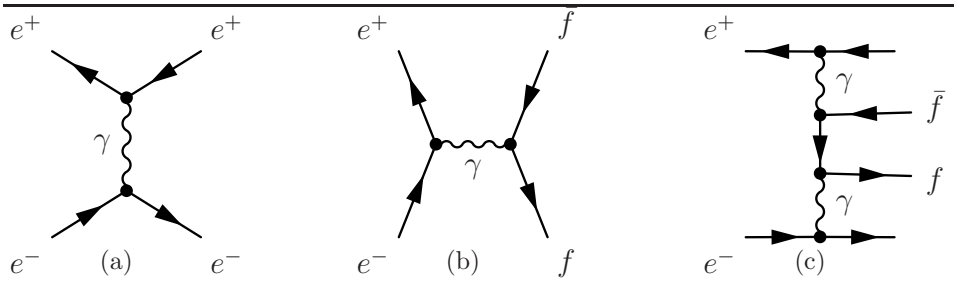

Figure 4.1: Feynman diagrams demonstrating the possible background production of any τ event. (a) t-channel Bhabha scattering. (b) e^+e^- annihiliation and subsequent fermion pair production where $f \in \{e^-, \mu^-, \tau^-, u, d, c, s\}$. (c) Two-photon event, where $f \in \{e^-, \mu^-, \tau^-, u, d, c, s\}$.

particles to one of two τ candidates. Events with the following properties meet the Tau1N selection [16]:

- Pass background filters designed to reject backgrounds from beam-gas interactions;
- Number of charged tracks < 10;
- Number of neutrals in each hemisphere (with Energy $> 50\,\text{MeV}$) < 6;
- Topology requirement of Good Tracks Very Loose (GTVL) 1-N ($N \geq 3$). (For a charge track to be in the Good Tracks Very Loose (GTVL) list, it is required to have the properties listed in Table 4.3); and
- Total event mass $< 3\,\text{GeV}/c^2$[1].

As mentioned earlier, τ pairs are produced back-to-back in the e^+ e^- centre of momentum frame. This allows the event to be divided into two hemispheres by a plane perpendicular to the thrust axis. Thrust is defined as,

$$T = \max_{\vec{A}} \frac{\sum_{i=1}^{N} |\vec{A} \cdot \vec{P_i}|}{\sum_{i=1}^{N} \|\vec{P_i}\|} \tag{4.2}$$

[1]The combined mass of all particles, neutral and charged.

Minimum Transverse Momentum	0.0 GeV/c
Maximum Momentum ($\|\mathbf{p}\|$)	10.0 GeV/c
Minimum Number of Drift Chamber Hits	0
Minimum Fit χ^2 Probability	0
Maximum DOCA in the x-y plane	1.5 cm
Minimum DOCA from the z-axis	-10 cm
Maximum DOCA from the z-axis	10 cm

Table 4.3: A track with the above properties is considered to be a *Good Track Very Loose*. DOCA is an abbreviation for Distance of closest approach.

where, $\overrightarrow{A} \in \mathbb{R}^3$ and $\|\overrightarrow{A}\| = 1$, N is the number of tracks and neutral clusters found in an event.

The thrust axis is the vector, $\overrightarrow{A}$ which maximizes T[2]. The direction of thrust, or thrust axis, cannot be unique, since $-\overrightarrow{A}$ also maximizes T, however this is the only common ambiguity in defining the thrust axis. The thrust axis is the direction which maximizes the sum of the longitudinal momenta of the system of particles. In the case of a pure hadronic event, the thrust axis corresponds to the axis along the primary $q\bar{q}$ pair produced from e^+e^- annihilation. In general pure hadronic events are more spherical in nature and commonly have a thrust value lower than dilepton events. In the case of a τ event, the thrust axis usually does not align with the τ's direction of travel.

In order to guarantee a high purity τ sample, we require that the magnitude of thrust must fall between 0.92 and 0.99 (see Figure 4.2). The lower bound eliminates much of the hadronic background and the upper bound removes Bhabhas and di-muon events.

[2]Thrust will always fall between $[0.5, 1]$. Larger thrust values correspond to events which might be described as being back to back (or events with a high collimation of the decay products into a region around a certain axis), while lower values correspond to events which are distributed more uniformly over the entire solid angle.

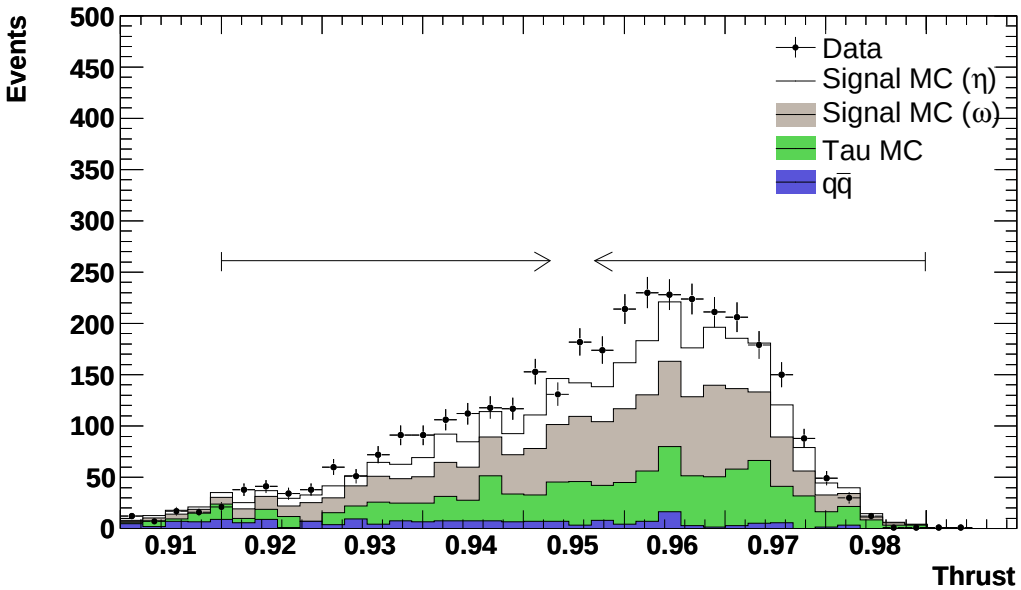

Figure 4.2: Plot of thrust with all cuts but the thrust cut applied ($0.92 \leq$ Thrust ≤ 0.99). The arrows indicate the region accepted by selection.

4.2.1 Topological Requirement

Topological branching ratios[3] are important for organizing experimental results. The phase space for a decaying τ lepton is large enough to create up to 12 pions, or a maximum of 11 charged hadrons. To date one-, three-, and five-prong[4] decays have been measured. It is not sufficient to simply count the number of tracks in the event because:

1. Photon Conversions ($\gamma \rightarrow e^+e^-$) caused by interactions in the detector material can generate fake tracks.

2. Dalitz Decays ($\pi^0 \rightarrow e^+e^-\gamma$), and other neutral hadronic decays to charged particles can generate spurious tracks.

3. Interactions in the detector material can lead to additional false tracks.

4. Multiple Scattering can cause a single track to be reconstructed as two.

5. Tracks can escape detection.[5]

Thus an event with a genuine $i - j$ topology can be reconstructed with a different topology.

We demand that the number of charged tracks in an event be six. In addition the event must have zero total charge, and each τ candidate must have the proper charge. For this analysis every event must have one charged track on the tag side and five charged tracks on the signal side (1-5 topology).

[3]The branching ratios of the τ lepton into a particular number of charged particles
[4]Prong stands for the signal of a charged track in the tracking chamber.
[5]e.g., If the charged particle heads down the beam pipe.

4.2.2 Tag Hemisphere Selection

To reduce the hadronic background, we require that one of the τ's decays leptonically ($\tau \to \nu_\tau \overline{\nu}_e$ or $\tau \to \mu \nu_\tau \overline{\nu}_\mu$). This decay in the 'tag' hemisphere must pass the following conditions:

1. The single charged tag track must pass either eMicroTight or muMicroTight selectors (see §A.1 and §A.2 for the track requirements of the electron or muon selectors).
2. $|\mathbf{p}^{\mathrm{TAG}}_{\mathrm{CMS}}| < 4.1\,\mathrm{GeV}/c$
3. $E^{\mathrm{TAG}}_{\mathrm{Neutral}} < 1\,\mathrm{GeV}$
4. $\mathrm{N}^{\mathrm{TAG}}_{\mathrm{Clusters}} < 2$

$|\mathbf{p}^{\mathrm{TAG}}_{\mathrm{CMS}}|$ is the momentum of the track in the tag hemisphere in the $e^+\ e^-$ centre-of-mass frame, and it is implemented to remove background from di-lepton events (see Figure 4.3). The cuts on number of neutrals and neutral energy in the tag hemisphere are to reduce $q\bar{q}$ background (see Figure 4.4 and Figure 4.5).

4.3 Signal Selection Requirements

To select $\tau^- \to 3\pi^- 2\pi^+ \pi^0 \nu_\tau$ decays we require:

- That there be 5 tracks in the signal hemisphere and that no track be identified as a conversion or be identified as an electron.
- That there is only one good π^0 in the signal hemisphere. (see §4.3.1)
- That the pseudomass of τ be less than $1.8\,\mathrm{GeV}/c^2$.

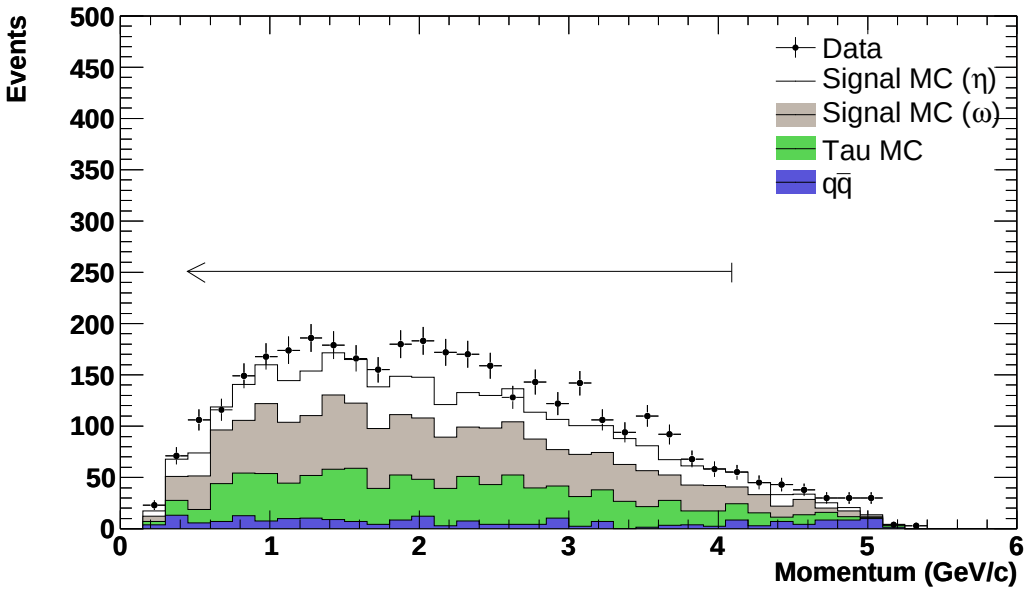

Figure 4.3: $|\mathbf{p}_{CMS}^{TAG}|$ Distribution with all cuts but the tag side centre-of-mass momentum cut applied ($|\mathbf{p}_{CMS}^{TAG}| < 4.1\,\mathrm{GeV}/c$).

In order to minimize the background from photon conversions, we have two requirements: a signal side electron veto and a signal side conversion veto. On the signal side we require that no tracks in the signal hemisphere pass the PID selector, eMicroVeryTight ($\mathrm{N}_{\mathrm{VeryTightElectrons}} = 0$, see Figure 4.6 and §A.1). This is designed to remove backgrounds that are not well-modeled in the Monte Carlo simulation including Bhabhas, photon conversions and Dalitz decays. Further, events are rejected if any pair of charged tracks is found to be consistent with a photon conversion ($\mathrm{N}_{\mathrm{conv}} = 0$)[6].

[6] see §B.2

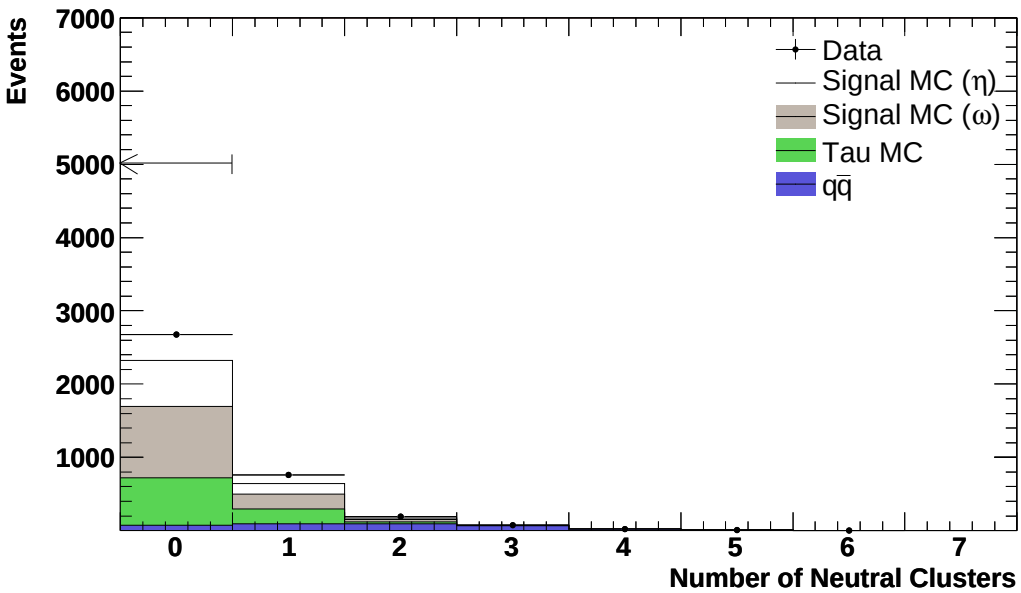

(a)

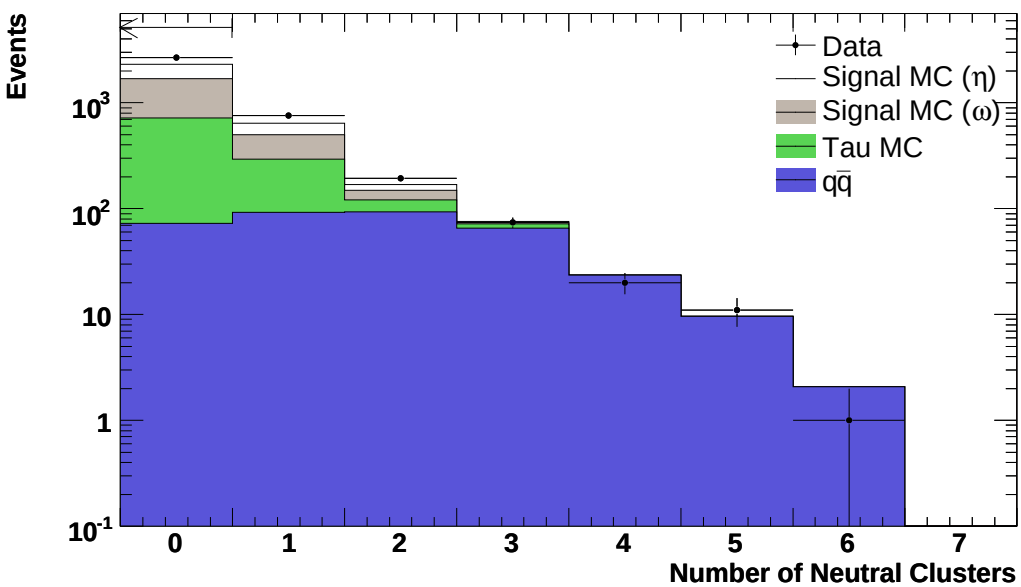

(b)

Figure 4.4: (a) The number of neutral clusters on the tag side with all selection cuts but the tag side requirement on number of neutral clusters (Number of Neutral Clusters < 2). (b) Plot of (a), but with logarithmic scale.

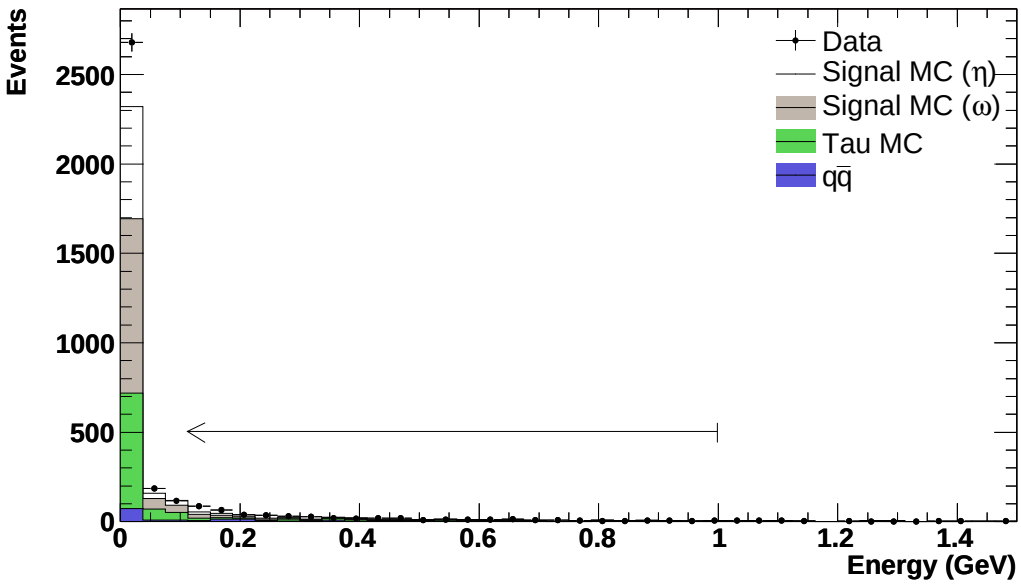

(a)

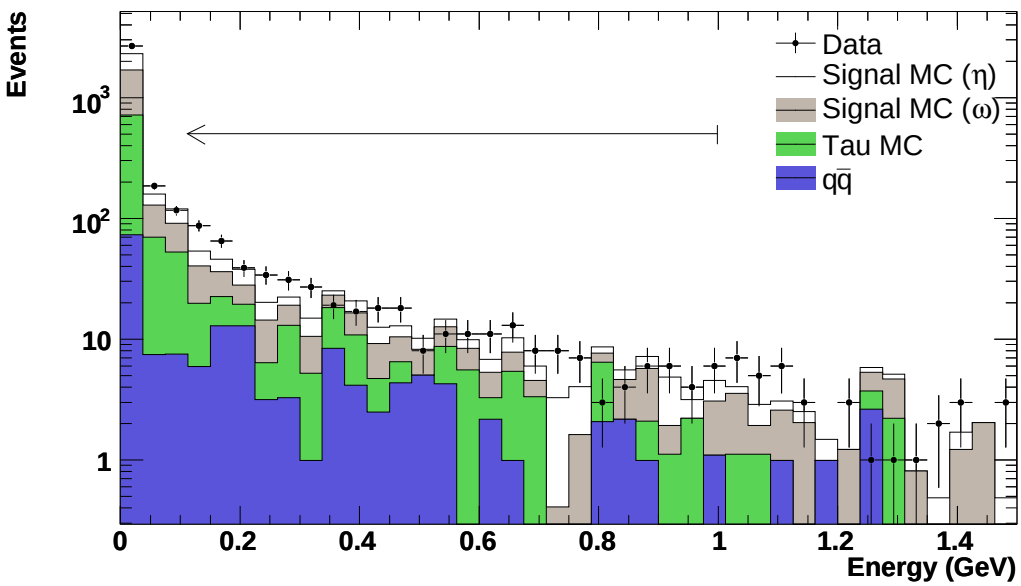

(b)

Figure 4.5: (a) The neutral energy on the tag side with all selection cuts but the tag side requirement on neutral energy (Neutral Energy $< 1\,\mathrm{GeV}$.). (b) Plot of (a), but with logarithmic scale.

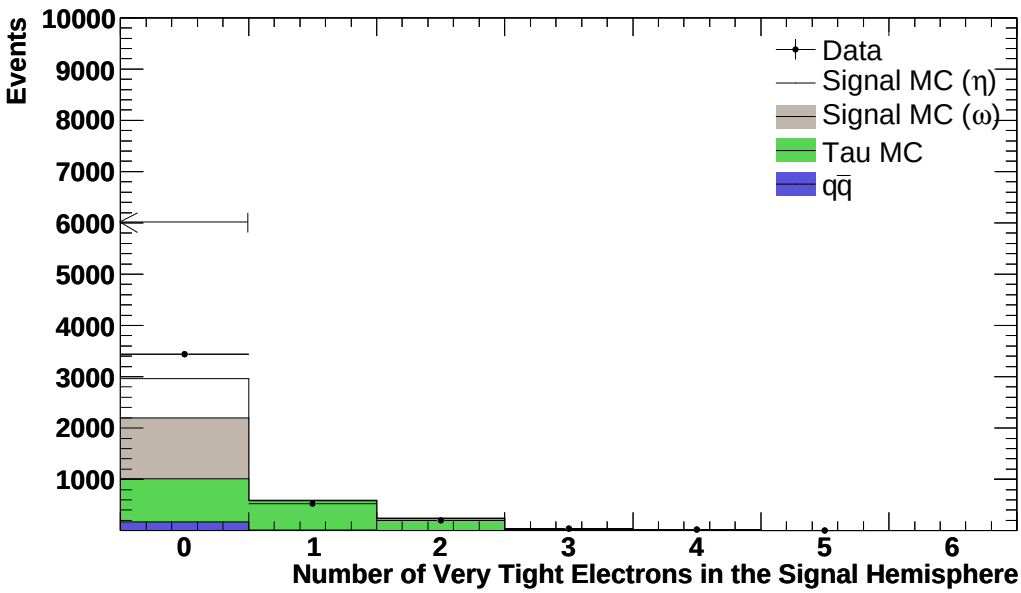

(a)

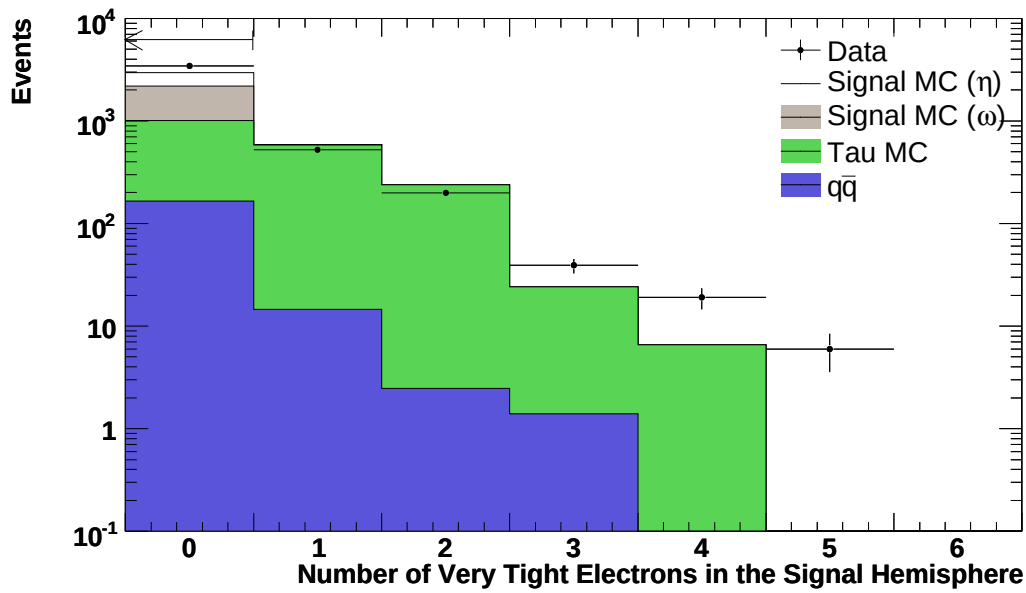

(b)

Figure 4.6: (a) The number of electrons in the signal hemisphere with all selection cuts but the requirement on the number of very tight electrons. (b) Plot of (a), but with a logarithmic scale.

4.3.1 π^0 Reconstruction

In τ hadronic decays a large number of π^0 mesons may be produced. π^0 mesons decay predominantly to two photons. The π^0 mesons have to be reconstructed from the energy deposits found in the electromagnetic calorimeters. Lists of π^0's are constructed by combining pairs of 'bumps' (entries in the *BABAR* `CalorNeutral` List). These bumps correspond to neutral energy deposits in the electromagnetic calorimeter of more than 30 MeV that are not associated with any charged particle candidates[7]. Additional quality cuts are imposed on neutrals before they are used to construct π^0's.

A subset of the π^0's are selected from the `pi0AllLoose` list by optimizing various cuts in order to select a purer sample, while maintaining a high efficiency. The `pi0AllLoose` list suffers from contamination due to background photons, detector noise, hadronic split-offs, and combinatorial background from π^0 s being created from many different combinations of photons (see §B.1 for `pi0AllLoose` list definition). We require, that a π^0 candidate consists of two distinct clusters[8] in the electromagnetic calorimeter that are not associated with any track. Each cluster is required to have localized energy deposit of at least 50 MeV. Additional requirements are imposed on the number of crystals registering hits; the lateral moment of the cluster; and the location of the crystal to ensure high quality photons. A π^0 energy ($E^0_\pi > 250\,\text{MeV}$) cut is used to reduce the of contamination from fake π^0's.

When two π^0's have a common daughter, we select the photon combination with the smallest $\chi^2 = \left(\frac{m_{\gamma\gamma}-m_{\pi^0}}{\sigma_{\gamma\gamma}}\right)^2$, where $\sigma_{\gamma\gamma}$ is the effective resolution of the combined photons and $m_{\gamma\gamma}$ is the invariant mass of the π^0 candidate. We also impose the addi-

[7]Merged π^0 candidates are constructed from a single high-energy neutral energy deposit.

[8]Merged π^0's, or π^0 made from only one EMC cluster, make up just over 1% of the π^0 candidates [17]. As such, this restriction on the type of π^0 s improves the quality of the average candidate, while not drastically reducing the number of selected events.

tional restriction that only one π^0 candidate can be found in the signal hemisphere.

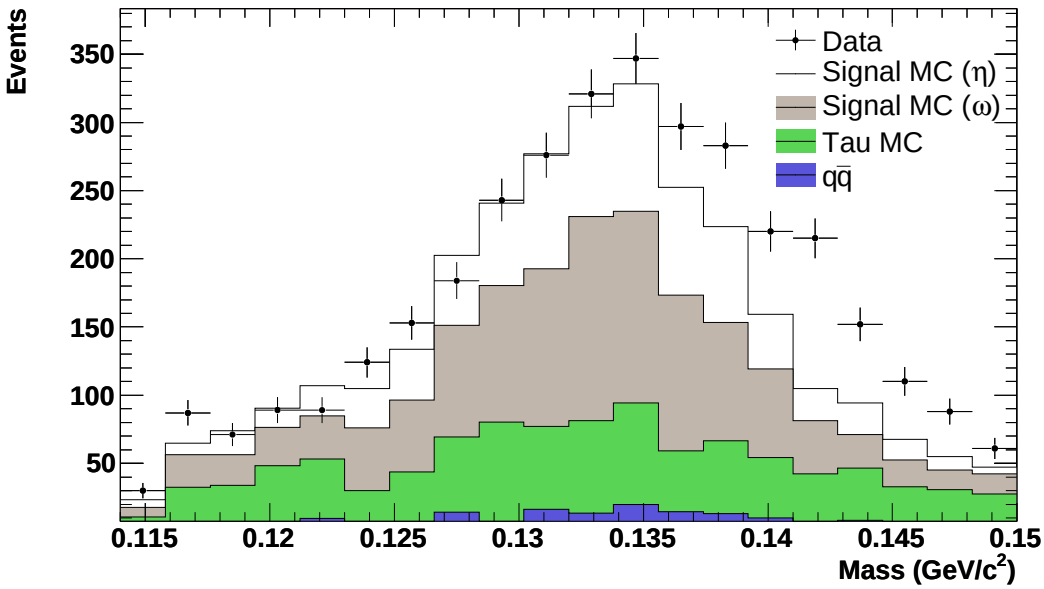

Figure 4.7: Invariant mass of the $\gamma\gamma$ candidate ($m_{\gamma\gamma}$) with all cuts applied.

4.3.2 τ Mass Requirement

One of the key variables for reconstructing a $\tau^- \to 3\pi^- 2\pi^+ \pi^0 \nu_\tau$ decay is the invariant mass of the observed particles ($3\pi^-$ $2\pi^+$ π^0). The reconstructed mass is expected slightly below the τ mass due to the omission of the ν_τ, which escapes detection. The background from generic τ events is a broad distribution with some events being found above the τ mass. Hadronic events, on the other hand typically have a higher mass which provides a mechanism to separate signal events from hadronic background.

The invariant mass can be calculated for the: mass of the 5π system ($m_{5\pi}$), mass of the $5\pi\pi^0$ system ($m_{5\pi\pi^0}$), and pseudomass (m_{pseudo}).

The pseudomass is a powerful variable for reducing $q\bar{q}$ background. In a hadronic τ decay, the mass of the τ lepton is related to the 4-momentum of the hadronic system

by:

$$\begin{aligned} m_\tau^2 &= (p_\tau)^2 \\ &= E_\tau^2 - (\mathbf{p}_{\rm had})^2 - E_{\nu_\tau}^2 - 2|\mathbf{p}_{\rm had}|E_{\nu_\tau}\cos(\phi) \\ &= E_\tau^2 - (\mathbf{p}_{\rm had})^2 - (E_\tau - E_{\rm had})^2 - 2|\mathbf{p}_{\rm had}|(E_\tau - E_{\rm had})\cos(\phi) \end{aligned}$$

where, $p_\tau(p_{\rm had})$, $\mathbf{p}_\tau(\mathbf{p}_{\rm had})$, and $E_\tau(E_{\rm had})$ the 4-momentum, 3-momentum, and Energy of the τ (or hadronic system). If we consider the decay in the centre-of-momentum system, the τ energy can be taken to be the beam energy. Assuming that the mass of the ν_τ is negligible, then the mass of the τ lepton can be reconstructed if the angle ϕ between the direction of the ν_τ and the hadronic system is known. The exact limit on ϕ depends on the $m_{\rm had}$. We define the pseudomass of the hadronic system, $m_{\rm pseudo}$ by taking ϕ to be zero [9, 18]. Pseudomass gives the true mass when $\phi = 0$ and is smaller than the true mass in any other case. Further, details of the shape of the distribution are determined by the dynamics of the decay with a general tendency that the more massive the hadronic system, the closer the pseudomass is to the τ mass [18].

It is clear from Figure 4.10 that $m_{\rm pseudo}$ provides a considerably better separation of a signal event from $q\bar{q}$ and hadronic τ background when compared to $m_{5\pi}$ and $m_{5\pi\pi^0}$ mass (Figures 4.8 and 4.9, respectively). We therefore impose the restriction that $m_{\rm pseudo} < 1.8\,{\rm GeV}/c^2$.

4.4 Results

We are left with 3440 candidate events in the data after all selections have been applied. The total number of background events in the Monte Carlo samples that pass the selection are listed in Table 4.4.

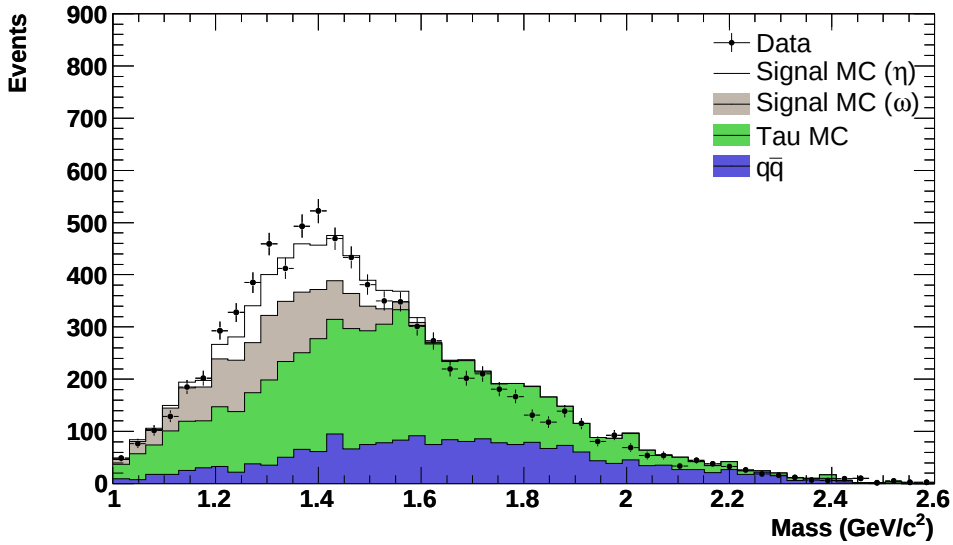

Figure 4.8: Invariant mass of the $3\pi^-\ 2\pi^+$ system in the signal hemisphere after all other selection criteria (except the mass requirement) are applied.

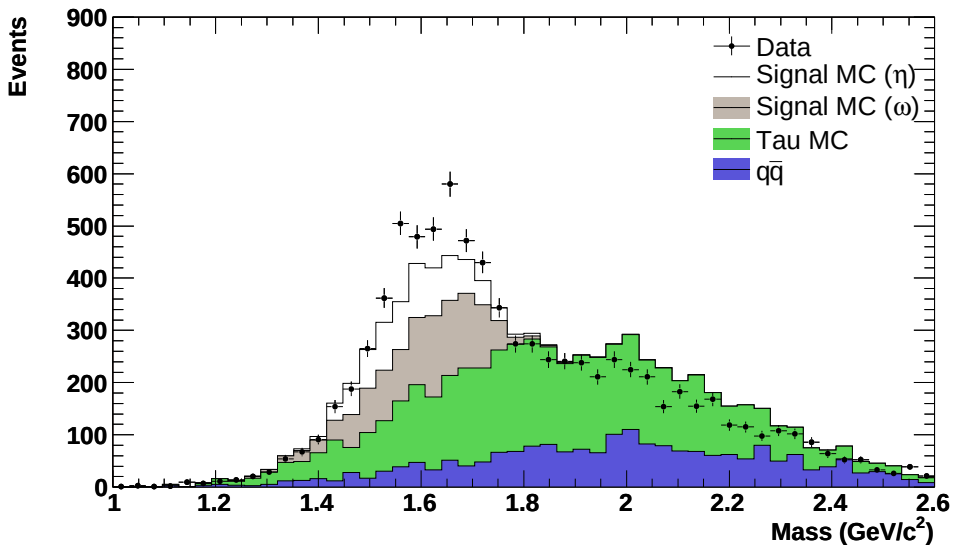

Figure 4.9: Invariant mass of the $3\pi^+\ 2\pi^-\ \pi^0$ system ($m_{5\pi\pi^0}$) in the signal hemisphere after all other selection criteria (except the mass requirement) are applied.

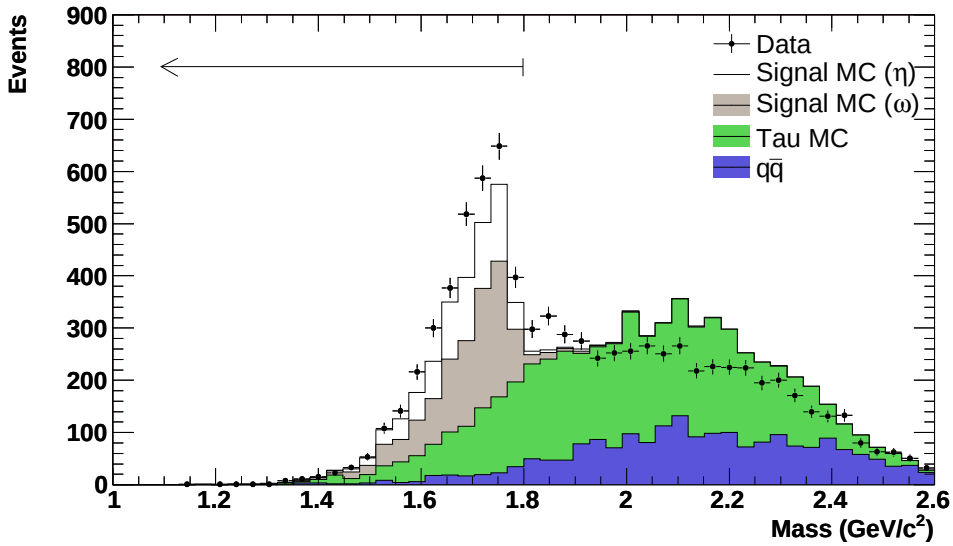

Figure 4.10: Pseudomass of the $3\pi^+\ 2\pi^-\ \pi^0$ system (m_{pseudo}) in the signal hemisphere after all other selection criteria (except the mass requirement) are applied.

Background Type	N_{selected}
τ	795
$c\bar{c}$	118
uds	28
$B^0\ \overline{B}^0$	2
$B\ \overline{B}$	0
Signal Type	
$f_1(1285)\pi^-\nu_\tau \to \pi^-\pi^+\pi^-\eta\nu_\tau$	4518
$f_1(1285)\pi^-\nu_\tau \to (\pi a_0(980))\pi^-\nu_\tau \to \pi^-\pi^+\pi^-\eta\nu_\tau$	4499
$\pi^-\pi^+\pi^-\eta\nu_\tau$	4465
$\pi^-\pi^+\pi^-\omega\nu_\tau$	3013

Table 4.4: Number of Background Events Passing Selection. τ is all generic τ Monte Carlo, excluding $\tau^- \to 3\pi^-2\pi^+\pi^0\nu_\tau$. These values do not include scaling corrections (see §4.1 and §5.6.7).

4.4.1 Primary Backgrounds

Backgrounds found in the selected sample can be categorized under the decays in Table 4.5.

Mode	Events	Contamination
$\tau^- \to 3\pi^- 2\pi^+ \nu_\tau$	251	6.5%
$\tau^- \to (\mathrm{X})^- \mathrm{n}(\pi^0)\nu_\tau$	424	10.9%
Other τ decays	120	3.1%
Total		20.5%

Table 4.5: The largest contributors of background as estimated by the Monte Carlo. Where $(\mathrm{X})^-$) is either one or three charged hadrons (pions or kaons).

Chapter 5

Results

The branching fraction for $\tau^- \to \pi^-\pi^+\pi^-\eta\nu_\tau$ decay mode is calculated by equation (2.10). We restate the equation for determination of this branching fraction in the following form,

$$\mathcal{B}(\tau^- \to \pi^-\pi^+\pi^-\eta\nu_\tau) = \frac{\mathrm{N}_{sig} - \mathrm{N}_{q\bar{q}+\tau}}{2\mathrm{N}_{\tau\tau}} \frac{1}{\epsilon} \frac{1}{\mathcal{B}(\eta \to \pi^+\pi^-\pi^0)} \tag{5.1}$$

where, $\mathrm{N}_{\tau\tau}$ is the number of τ pairs, ϵ is the measured selection efficiency, $\mathcal{B}(\eta \to \pi^+\pi^-\pi^0)$ is the branching fraction of $\eta \to \pi^+\pi^-\pi^0$ ($22.7 \pm 0.4\%$ [1]), $\mathrm{N}_{q\bar{q}+\tau}$ is the estimate on the amount of peaking background due to $q\bar{q}$ and τ events, and N_{sig} is the number of η candidates after selection. In the following sections we descibe how these parameters are measured. In §5.6 we present our estimates on the systematic errors associated with this measurement.

The selection criteria outlined in Chapter 4 is designed to select $\tau^- \to 3\pi^-\ 2\pi^+\ \pi^0\ \nu_\tau$ events. Our goal is to measure, the $\tau^- \to \pi^-\pi^+\pi^-\eta\nu_\tau$ branching fraction. Although η mesons predominately decay to neutral final states, we only consider the final state $\pi^+\pi^-\pi^0$ (see Table 5.1).

To determine the number of η mesons it is necessary to fit the $\pi^+\pi^-\pi^0$ invariant mass distribution (shown in Figure 5.1). Note that there are six possible combinations

η **Decay Modes**	Branching Fraction (Γ_i/Γ)
neutral modes	$71.9 \pm 0.5\%$
2γ	$39.98 \pm 0.26\%$
$3\pi^0$	$32.51 \pm 0.28\%$
charged modes	$28.0 \pm 0.5\%$
$\pi^+\ \pi^-\ \pi^0$	$22.7 \pm 0.4\%$
$\pi^+\ \pi^-\ \gamma$	$4.69 \pm 0.11\%$

Table 5.1: η Branching Fraction [1, Meson Summary Table]

of $\pi^+\pi^-\pi^0$ in the $3\pi^-\ 2\pi^+\ \pi^0$ final state. As can be seen in the Figure 5.1b there are backgrounds from a number of sources. The white histogram is $\tau \to \pi^-\pi^+\pi^-\eta\nu_\tau$ Monte Carlo prediction where there is an η peak as well as background from incorrect $\pi^+\pi^-\pi^0$ combinations (this is known as combinatoric background). There is also background from other τ decays and $q\bar{q}$ events. We do not expect any η mesons from the other τ decays.

5.1 Data and Monte Carlo Fits

The η resonance shape is normally described by a Breit-Wigner (see §2.4) with the full width being $1.30 \pm 0.07\,\mathrm{keV}/c^2$ [1]. However, since the experimental mass resolution of the *BABAR* detector is estimated to be $5\,\mathrm{MeV}/c^2$ the measured width of the η should be dominated by the intrinsic detector resolution and the resonance line shape should be described by a Gaussian resonance line shape (see Equation (5.2)).

$$G(m; m_0, \sigma, \mathrm{N}_0) = \frac{\mathrm{N}_0}{\sqrt{2\pi}\sigma} e^{-\frac{(m-m_0)^2}{2\sigma^2}}, \tag{5.2}$$

where m is the independent variable, m_0 is the mean of the Gaussian and should be equal to the η mass, σ is the resolution parameter and should be related to the intrinsic detector resolution, and N_0 is the normalization parameter and is to the

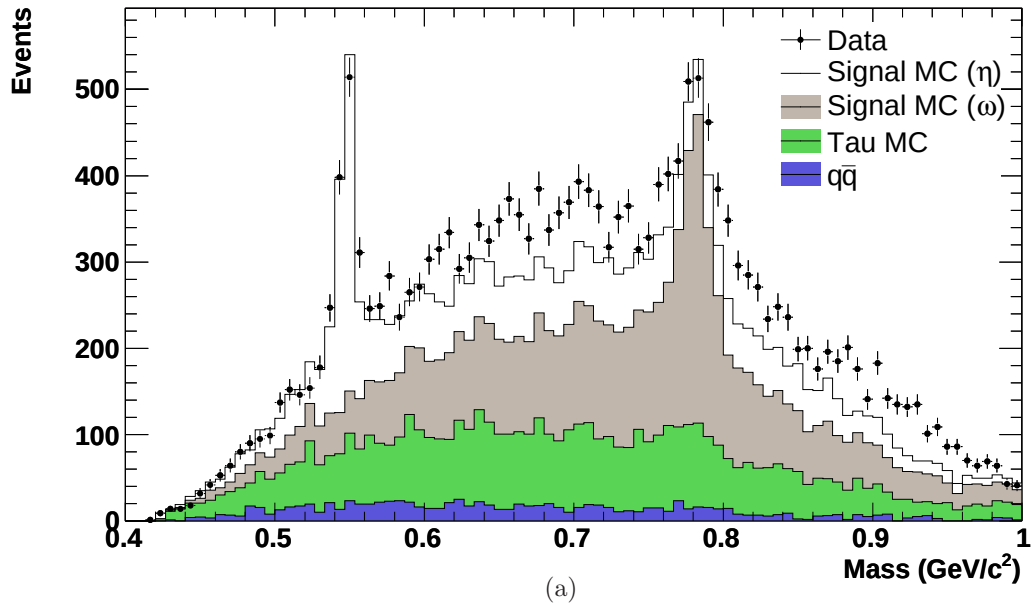

(a)

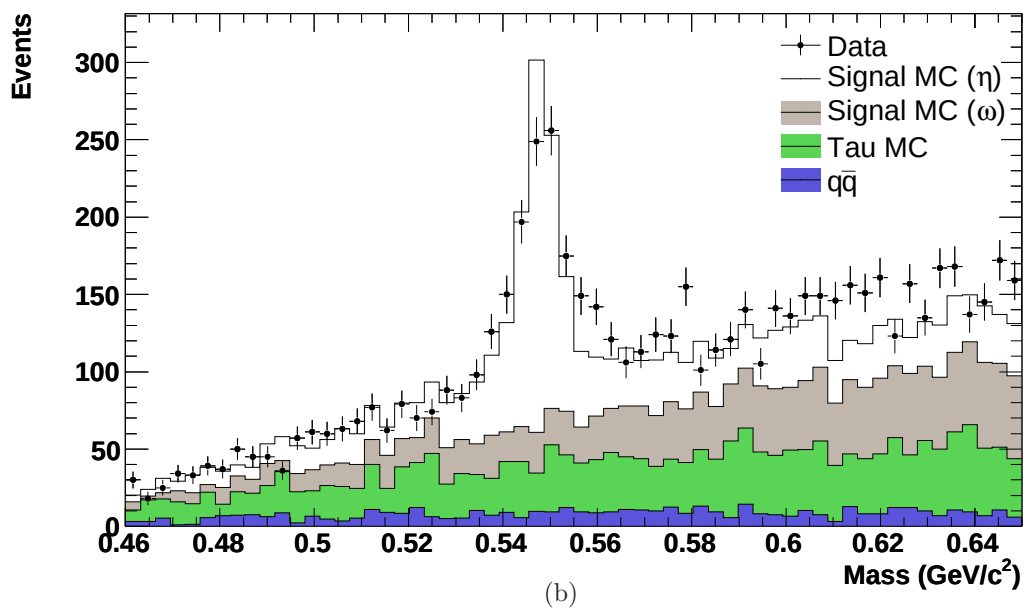

(b)

Figure 5.1: Mass of the π^+ π^- π^0 combinations in the signal hemisphere after all selection criteria are applied. The lower plot only shows the region around the η mass peak.

number of events in the peak.

The invariant mass distribution of the $\pi^+\pi^-\pi^0$ system is fitted using a second-order polynomial (to describe the background) and a Gaussian (to model the peak). The fit range is from 460 MeV/c^2 to 650 MeV/c^2. The fitting procedure uses a binned χ^2 fit to determine parameters. The parameters for the second order polynomial are constrained to be within three standard deviations of the parameter determined in a sideband fit[1].

5.2 N_η

We have 3440 candidate $\tau^- \to 3\pi^-2\pi^+\pi^0\nu_\tau$ events after all selections have been applied. After fitting, we determine that are $N_\eta = 661 \pm 48$. The Gaussian parameters determined by the fit are listed in Table 5.2. The data fit is shown in Figure 5.2a.

Parameter	Fit Value (Data)
N_0	661 ± 48
σ	(5.74 ± 0.47) MeV/c^2
m_0	(548.1 ± 0.4) MeV/c^2
χ^2/ndf	$\frac{68}{54}$
	Fit Value (Monte Carlo)
N_0	3635 ± 72
σ	(3.78 ± 0.08) MeV/c^2
m_0	(547.42 ± 0.08) MeV/c^2
χ^2/ndf	$\frac{385}{294}$

Table 5.2: Fit Parameters for Data and Monte Carlo ($\tau^- \to \pi^-\pi^+\pi^-\eta\nu_\tau$).

The measured width of the Gaussian fit (σ) provides a measurement of the detector resolution. From the fits, the measured resolution is (5.74 ± 0.47) MeV/c^2 . This value is consistent with previous *BABAR* measurements.

[1]Using a second order polynomial to fit the peak sidebands - [excluding the peak region (520-570 MeV/c^2)].

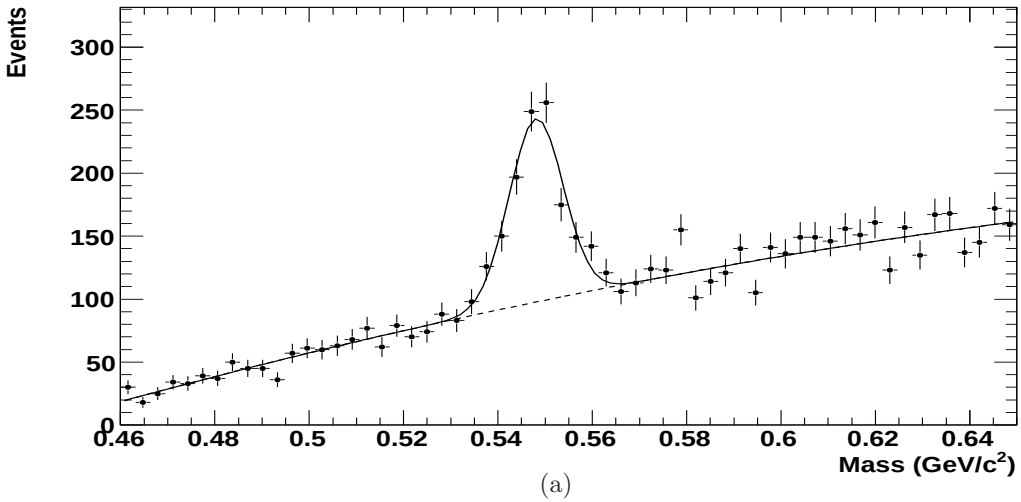

(a)

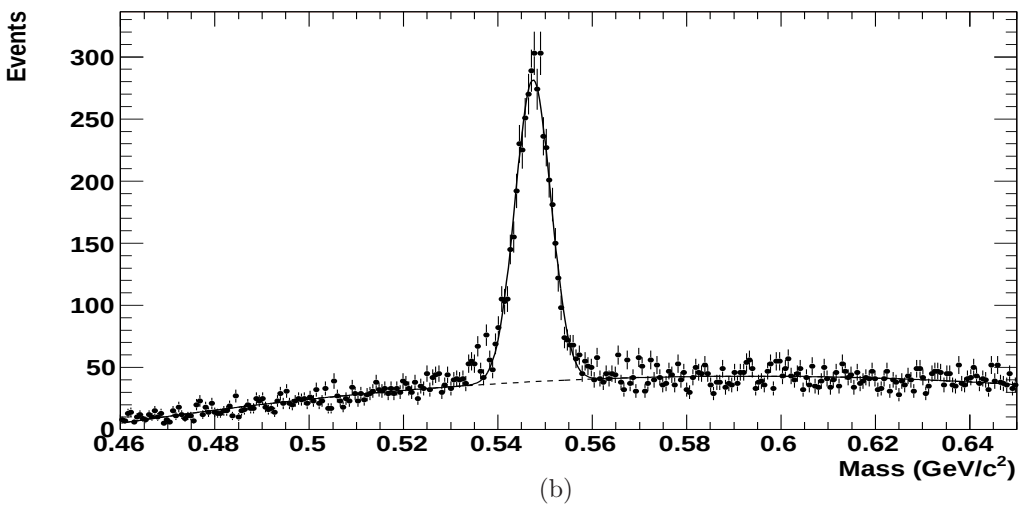

(b)

Figure 5.2: Reconstructed mass of π^+ π^- π^0 in the signal hemisphere. The data points are shown with error bars. There are a total of six entries per event. Both fits use a 2nd order polynomial to descibe the backgound and a Gaussian to describe the peak. (a) Data; (b) $\tau^- \to \pi^-\pi^+\pi^-\eta\nu_\tau$ Monte Carlo.

5.3 Selection Efficiency

We use the signal Monte Carlo sample ($\tau^- \to \pi^-\pi^+\pi^-\eta\nu_\tau$) to measure the efficiency of our selection criteria. The efficiency is defined as $\mathrm{N_{sel}}/\mathrm{N}_i$, where $\mathrm{N_{sel}}$ is the number

of events found after all selection criteria have been applied and N_i is the total number of generated Monte Carlo events (100,000). The selection efficiency for the various types of signal Monte Carlo are listed in Table 5.3. The efficiency includes corrections for differences in finding electrons and muons in data and Monte Carlo (see §5.6.7). The selection efficiency is calculated to be $(3.64 \pm 0.07)\%$, where the error is statistical. The fit is shown in Figure 5.2b.

Signal Type	Efficiency
$f_1(1285)\pi^-\nu_\tau \to \pi^-\pi^+\pi^-\eta\nu_\tau$	$(3.65 \pm 0.07)\%$
$f_1(1285)\pi^-\nu_\tau \to (\pi a_0(980))\pi^-\nu_\tau \to \pi^-\pi^+\pi^-\eta\nu_\tau$	$(3.57 \pm 0.07)\%$
$\pi^-\pi^+\pi^-\eta$	$(3.64 \pm 0.07)\%$

Table 5.3: Selection efficiency of signal modes ($\tau^- \to \pi^-\pi^+\pi^-\eta\nu_\tau$).

5.4 $N_{q\bar{q}+\tau}$ Peaking Background

The Monte Carlo also indicates that there is no contribution to the η peak from $q\bar{q}$ events. It is estimated that the amount of τ and $q\bar{q}$ background that contaminates the η peak to be 0 ($N_{q\bar{q}+\tau} = 0$). Figure 5.3a shows the result of a fit to the side band region of all $q\bar{q}$ and generic τ backgrounds. If we include a Gaussian to describe a potential peak, (see Figure 5.3b) with the mean and resolution parameters being equal to the value found by the signal Monte Carlo, we find that the number of background events is 4.1 ± 13.4, which is consistent with zero.[2]

5.5 $\mathcal{B}(\tau^- \to \pi^-\pi^+\pi^-\eta\nu_\tau)$

The number of τ pairs ($N_{\tau\tau}= 2.13\times10^8$) is defined to be the product of the integrated luminosity and τ pair production cross section. The efficiency (ϵ) was determined

[2]In Appendix C.1 $q\bar{q}$ and τ backgrounds are plotted separately.

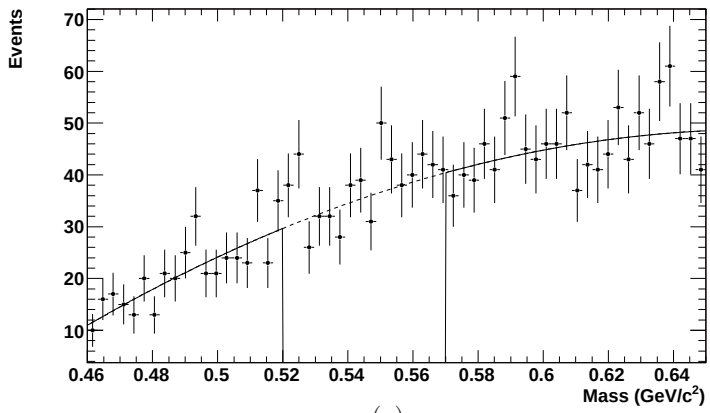

(a)

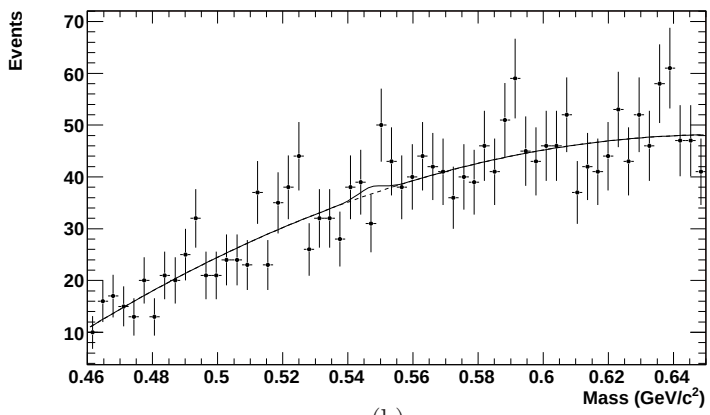

(b)

Figure 5.3: (a) Using the Monte Carlo, all contributing background in the η signal region have been combined and fit with a second order polynomial, which excludes points found between 520-570 MeV/c^2. (b) Using the Monte Carlo, all contributing background in the η signal region have been combined and fit with a second order polynomial to describe the background and Gaussian to describe any possible peak. The mean and resolution parameter of the Gaussian have been fixed to the values measured using the signal Monte Carlo fit. There is no observable peaking background in the η region.

from the signal Monte Carlo and was found to be (3.64±0.07)%. The $\mathcal{B}(\eta \to \pi^+\pi^-\pi^0)$ is the branching fraction of $\eta \to \pi^+\pi^-\pi^0$ ($22.7 \pm 0.4\%$ [1]), peaking background was not observed ($\mathrm{N}_{q\overline{q}+\tau} = 0$). Using the fit results and our systematic error estimates,

we calculate $\mathcal{B}(\tau^- \to \pi^-\pi^+\pi^-\eta\nu_\tau)$=$(1.88 \pm 0.14 \pm 0.11) \times 10^{-4}$ where the first error is the statistical error and the second error is the systematic error. Systematic errors are discussed in the next section (§5.6).

5.6 Systematic Errors

The largest systematic error is track reconstruction uncertainty (3.1%). Remaining systematic errors are listed in Table 5.4, and include terms for the π^0 selection efficiency, uncertainty in the fit result of the η meson, possible η contamination due to improperly modelled $q\bar{q}$ and τ Monte Carlo, luminosity and τ production cross section uncertainty.

Error Type	Error (%)
Tracking Efficiency	3.1
π^0 Selection Efficiency	3.0
η fit	3.0
$N_{\tau\tau}$	2.3
$N_{q\bar{q}+\tau}$ Peaking Background	2.2
MC efficiency	2.1
$\mathcal{B}(\eta \to \pi^+\pi^-\pi^0)$	1.8
Lepton PID	1.6
Total	6.9

Table 5.4: Estimates on the systematic errors associated with the branching fraction of $\tau^- \to \pi^-\pi^+\pi^-\eta\nu_\tau$.

5.6.1 Tracking Efficiency

The error on tracking efficiency for GTVL tracks has been determined (by the *BABAR* tracking efficiency working group) to be 1.2% per track for $p_T < 0.3\,\text{GeV}$ and 0.5% per track for $p_T > 0.3\,\text{GeV}$ [19]. These uncertainties are the current best estimates

of the error on the tracking efficiency. The total tracking efficiency is given by

$$\epsilon_{\mathrm{t}} = \epsilon_h^5 \epsilon_l \,, \tag{5.3}$$

where $\epsilon_h = 0.97 \pm 0.005$ and $\epsilon_l = 0.97 \pm 0.012$ and are the efficiencies on the high and low momentum tracks, respectively. We include the additional assumption that the errors are 100% correlated, and add them linearly. This results in the systematic error, due to tracking inefficiencies on the branching ratio being 3.1%.

5.6.2 π^0 Selection Efficiency

We use 3.0% systematic error for π^0 selection efficiency, which is recommended by the *BABAR* neutrals analysis working group [17, 20].

5.6.3 η Fit

We assign an error which is associated with the fitting of the $\pi^+\pi^-\pi^0$ invariant mass. The error is associated with variations in the final $\tau^- \to \pi^-\pi^+\pi^-\eta\nu_\tau$ branching fraction when different fitting methods are used. If the mean parameter of the Gaussian is fixed to the η mass there is a decrease of 1.5% in the normalization coefficient[3]. Changing the fit function to a Novosibirsk[4] causes only a negligible increase in the number of events. We also include a contribution, resulting from using different mass binning, background functions, and requiring a fixed resolution parameter. We assign a conservative systematic error of 3% which we attribute to the η fit and parameter choice.

[3]The number of observed events becomes 651 ± 47

[4]A Novosibirsk function is often described as an asymmetric gaussian. It has an additional tail parameter. This is the fit function used in [21].

5.6.4 Luminosity and Cross Section Errors

The number of τ pairs is equal to the product of the integrated luminosity and cross section. The error on the number of τ pairs is

$$\Delta \mathrm{N}_{\tau\tau} = (\Delta \mathscr{L}_{\mathrm{integrated}}) \oplus (\Delta \sigma_{\tau\tau}) \tag{5.4}$$

where $\oplus$ means errors are added in quadrature. The *BABAR* τ analysis working group uses a 2.3% systematic error on $\mathrm{N}_{\tau\tau}$.

5.6.5 MC Efficiency

These values are the statistical errors from the η fit on the signal Monte Carlo.

5.6.6 $\mathrm{N}_{q\bar{q}+\tau}$ Peaking Background

The number of η observed due to background contamination was 4.1 ± 13.4. This value is consistent with zero. We assign a 2.2% systematic error relating to the statistical error on the fit to determine the number of η mesons due to background contamination ($2\% \approx 13.4/661$), this number is in agreement with an independent investigation of the behaviour of the $\pi^+ \pi^- \pi^0$ mass spectrum for events found above m_τ pseudomass cut (see C.2).

5.6.7 Lepton PID

There is an observed discreption between the efficiency of identifying electrons and muons in data and Monte Carlo (this introduces the additional systematic error which can be associated with lepton particle identification). The systematic error on the particle identification of the tag particle is evaluated using the *BABAR* PID tables. The difference between the efficiency in the data and Monte Carlo for electrons identified with `eMicroTight` selection was found to be a uniform correction of 0.99 ± 0.01. For

muons selected with the `muMicroTight` selection the relative efficiency correction is found to be 0.90 ± 0.025. We assign an a systematic error of 1.6% to the branching ratio for the combined electron and muon selection PID efficiencies.

Chapter 6

Summary

The $\tau \to \pi^-\pi^+\pi^-\eta\nu_\tau$ decay using the $\eta \to \pi^+\pi^-\pi^0$ mode is studied with data taken by the *BABAR* detctor. The branching fraction of $\tau \to \pi^-\pi^+\pi^-\eta\nu_\tau$ is measured to be $(1.88 \pm 0.14 \pm 0.11) \times 10^{-4}$ where the first error is statistical and the second error is systematic. This measurement is in agreement with the PDG value of $(2.3 \pm 0.5) \times 10^{-4}$ [1] and the *BABAR* measurement of $(1.84 \pm 0.09 \pm 0.13) \times 10^{-4}$ using the $\eta \to \gamma\gamma$ decay channel [21].

Bibliography

[1] Yao, W.-M. et. al. Review of particle physics. *Journal of Physics G*, 33:1+, 2006.

[2] The BABAR Collaboration. The BABAR Detector. *Nuclear Instrument and Methods In Physics Research*, A479:1, 2002.

[3] P. F. Harrison and H. R. Quinn, editors. *The BaBar physics book: Physics at an asymmetric B factory*. The BABAR Collaboration, 1998.

[4] D. Griffiths. *Introduction to Elementary Particles*. John Wiley & Sons, New York, 1987.

[5] F. Halzen and A.D. Martin. *Quarks and Leptons: An Introductory Course in Modern Particle Physics*. John Wiley & Sons, New York, 1st edition, 1984.

[6] I.J.R. Aitchison and A.J.G. Hey. *Gauge Theories in Particle Physics, Volume 1: From Relativistic Quantum Mechanics to QED*. Taylor & Francis, New York, 3rd, revised edition, 2002.

[7] Ta Pei Cheng and Ling Fong Li. *Gauge theory of elementary particle physics*. Oxford University Press, Toronto, 1st edition, 1984.

[8] M. L. Perl et. al. Evidence for anomalous lepton production in $e^+ - e^-$ annihilation. *Phys. Rev. Lett.*, 35(22):1489–1492, Dec 1975.

[9] A. Stahl. *Physics with Tau Leptons*. Springer, New York, 1st edition, 2000.

[10] J. H. Kuehn. The tau lepton: Particle physics in a nutshell. *Nuclear Physics B - Proceedings Supplements*, 76:21, 1999.

[11] W. Greiner, S. Schramm, and E. Stein. *Quantum Chromodynamics*. Springer-Verlag, Berlin, 2nd edition, 2002.

[12] Stanford University. SLAC Virtual Visitor Center - Accelerator Form and Function. http://www2.slac.stanford.edu/vvc/accelerator.html, 2006.

[13] S. Jadach, B. F. L. Ward, and Z. Was. The precision Monte Carlo event generator KK for two-fermion final states in e^+e^- collisions. *Comput. Phys. Commun.*, 130:260–325, 2000.

[14] Z. Was. Tauola the library for tau lepton decay, and kkmc/koralb/koralz/... status report. *Nuclear Physics B - Proceedings Supplements*, 98:96, 2001.

[15] A. Ryn and D. Lange. The evtgen package for simulating particle decays, 1998. Paper presentated at CHEP, http://www.hep.net/chep98/PDF/160.pdf.

[16] S. Banerjee et. al. CM2 skims for $e^+e^- \rightarrow \mu^+\mu^-$ and $e^+e^- \rightarrow \tau^+\tau^- events$. BAD #760, Version 1 (*BABAR* internal analysis document), 2003.

[17] J. Williams. The tauAWGpi0 list: π^0s for tau analyses. BAD #896, Version 1 (*BABAR* internal analysis document), 2005.

[18] G. Abbiendi and the OPAL collaboration. A measurement of the τ mass and the first CPT test with τ leptons. *Physics Letters B*, 492:23, 2000.

[19] B. Aubert and the *BABAR* Collaboration. Study of the tau- –> 3h-2h+nu decay. *Physical Review D*, 72:072001, 2005.

[20] M. Allen et. al. A measurement of π^0 efficiency using $\tau \rightarrow \rho\nu$ and $\tau \rightarrow \pi\nu$ decays. BAD #870, Version 2 (*BABAR* internal analysis document), 2004.

[21] R. Sobie and M. Lewczuk. Study of tau to 3 pion and eta decay. BAD # 1603, Version 14 (*BABAR* internal analysis document), 2007.

Appendix A

A.1 Electron Tight and Very Tight Selector

Electron candidates are identified by the ratio of 'bump' energy in the electromagnetic calorimeter to track momentum, E_{EMC}/p. In addition, the track must have a measured mean ($\mathrm{d}E/\mathrm{d}x$) in the DCH consistent with the electron hypothesis. The lateral[1] and azimuthal[2] shape of the EMC shower and the observed Cherenkov angle in the DIRC must be consistent with an electron. See tables A.1 and A.2 for the full definitions of the `eMicroTight` and `eMicroVeryTight` selector definitions, respectively.

Electron identification efficiencies are around 90%, and the pion misidentification rates are below 0.3% for the `VeryTight` selection.

[1]The lateral moment of the cluster associated with this track, is given by the ratio of (1) to (2):

(1) Sum of energies of all but the 2 most energetic crystals, weighted by the square of distance to the cluster center.

(2) Sum of (1) and the energies of the 2 most energetic crystals, which are weighted by $(5\mathrm{cm})^2$ (5cm is the length scale of a crystal).

The lateral moment is a measure of the radial energy profile of the cluster, and is used to suppress clusters from electronic noise (low lateral moment) or hadronic interactions (high lateral moment).

[2]$|A_{4,2}|$ is absolute value of $(4,2)-$Zernike Moment of the associated EMC cluster. The $(4,2)$-Zernike Moment measures the azimuthal asymmetry of the cluster about its peak, can be used to distinguish between electromagnetic from hadronic showers.

E_{EMC}/p	$\in$	[0.75,1.3]
$\mathrm{N}_{\mathrm{crystals}}$	$>$	4
Lateral Moment	$\in$	[0.0,0.6]
$(\mathrm{dE/d}x)_{\mathrm{expected}} - (\mathrm{dE/d}x)_{\mathrm{measured}}$	$\in$	$(-3\sigma_{(\mathrm{dE/d}x)}, 7\sigma_{(\mathrm{dE/d}x)})$

Table A.1: Requirements for a track to pass the eMicroTight tag bit. $(\mathrm{d}E/\mathrm{d}x)$ and $\sigma_{(\mathrm{dE/d}x)}$ are the measurement and its associated error of energy lost per path length using only the drift chamber. $\mathrm{N}_{\mathrm{crystals}}$ is the number of crystals in the EMC which are above the threshold requirement for a hit detection and are in a 'nearest neighbour' geometry.

E_{EMC}/p	$\in$	[0.89,1.2]
$\mathrm{N}_{\mathrm{crystals}}$	$>$	4
Lateral Moment	$\in$	[0.1,0.6]
$\lvert A_{4,2}\rvert$	$<$	0.42
$(\mathrm{dE/d}x)_{\mathrm{expected}} - (\mathrm{dE/d}x)_{\mathrm{measured}}$	$\in$	$(-2\sigma_{(\mathrm{dE/d}x)}, 4\sigma_{(\mathrm{dE/d}x)})$
θ_c	$\in$	$(\theta_c^e - 3\sigma_{\theta_c}, \theta_c^e + 3\sigma_{\theta_c})$

Table A.2: Requirements for a track to pass the eMicroVeryTight tag bit. θ_c is the angle associated with the opening angle of the Cherenkov ring, and θ_c^e is the expected Cherenkov opening angle for an electron; σ_{θ_c} is associated error on the opening angle of the Cherenkov ring; $(\mathrm{dE/d}x)$ and $\sigma_{(\mathrm{dE/d}x)}$ are the measurement and its associated error of energy lost per path length using only the drift chamber. $\mathrm{N}_{\mathrm{crystals}}$ is the number of crystals in the EMC which are above the threshold requirement for a hit detection and are in a nearest neighbour geometry.

A.2 Muon Tight Selector

Muon candidates are identified by the measured number of hadronic interaction lengths traversed from the outer radius of the DCH through the IFR iron (n_λ), and the difference between measured and the predicted penetration depth for a muon of the same momentum and angle (Δn_λ). Hadronic showers are rejected by a combination of the average number of hit strips per IFR layer ($\bar{n}_{hits}$) and the variance of hits per RPC layer $\sigma_{n_{hits}}$.

To ensure that IFR hits are associated with a track, the χ^2 for the geometric match between the track extrapolation into the IFR and the RPC hits must be small (χ^2_{track}). In addition, the χ^2 of a polynomial fit to the RPC hits, χ^2_{fit} is required to be consistent with an isolated charge track.

For muons within the acceptance of the EMC there is an additional requirement that the calorimeter bump energy be consistent with a minimum ionizing particle. Pion misidentification rates are below 3% for the `Tight` selection. See tables A.3 for the full definitions of the `muMicroTight` selector definition.

E_{EMC}	$\in$	[0.05 GeV,0.4 GeV]
n^{IFR}_{layers}	$\geq$	2
$n\lambda$	$\geq$	2.2
$\Delta(n\lambda)$	$\in$	$(-1, +1)$
$\bar{n}_{hits}$	$<$	8
$\sigma_{n_{hits}}$	$<$	4
$\chi^2_{track}/n_{layers}$	$<$	5
χ^2_{fit}/n_{layers}	$<$	3

Table A.3: Requirements for a track to pass the muMicroTight tag bit. For candidates in the forward endcap, the number of hit IFR layers divided by the total number of layers between the first and last hit layers must be greater than 0.34 to reject beam background in the outermost layer.

Appendix B

B.1 Pi0AllLoose List

The basic and inclusive *BABAR* list is the `pi0AllLoose` List. It is made by adding the entries in the list of merged π^0 candidates in `MergedPi0Loose` list and the entries in resolved two cluster π^0 list, `Pi0LooseMass`.

The requirements for a pair of photons to be in `Pi0LooseMass` list are in table (B.1).

photon candidates	$\in$	`CalorNeutral` List
photon energy	$>$	30 MeV
photon lateral moment	$<$	0.8
reconstructed π^0 mass	$\in$	[0.100,0.160]
π^0 energy	$>$	0.2 GeV

Table B.1: All π^0 candidates are required to have the above properties in order to be included in the `pi0LooseMass` list.

B.2 Conversion Definition

Charged tracks from photon conversions in generic τ decays contribute to an increased multiplicity of the event and therefore contribute to the number of selected 1-5 candidate events. The standard *BABAR* conversion finder tries to combine pairs of

oppositely charged tracks to a common vertex. All conversion candidates are stored in the `gammaConversionDefault` list. However, if one of the following holds,

- $m_{ee} > 0.2\,\mathrm{GeV}/c^2$
- $m_{ee} > 0.005\,\mathrm{GeV}/c^2$ and $\mathrm{E}_{ee} > 1\,\mathrm{GeV}$

where, m_{ee} is the convsersion mass and E_{ee} is the energy of the conversion candidate, the last two requirements reduce the number of signal events rejected by the conversion algorithm. Plots of the mass of conversion (assuming both tracks are electrons), the radial distance of the conversion vertex from the interaction point, and the energy of the conversion are presented in figure B.1.

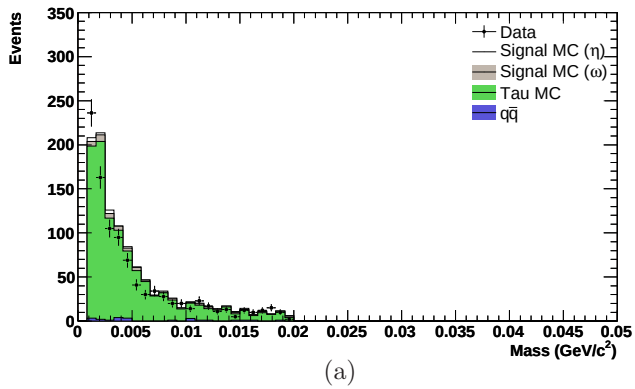

(a)

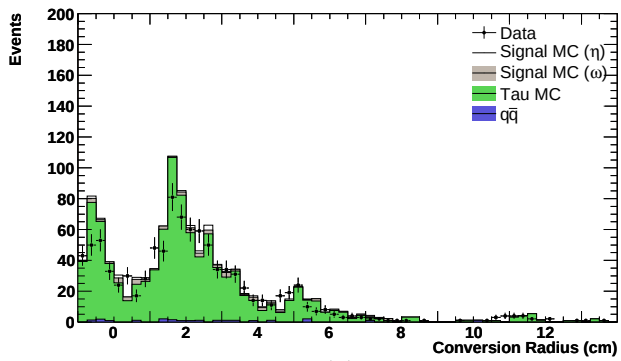

(b)

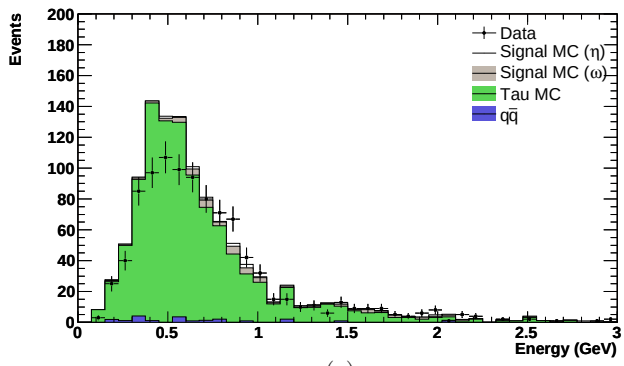

(c)

Figure B.1: (a) Mass of the conversion candidate. (b) Radial distance of the conversion vertex from the interaction point. (c) Energy of the conversion candidate. In the radial distance of the reconstructed materialization point for the pair conversion candidates, there are distinct peaks. These peaks correspond to conversions in the walls between various parts of the detector.

Appendix C

C.1 Background Seperated Modes

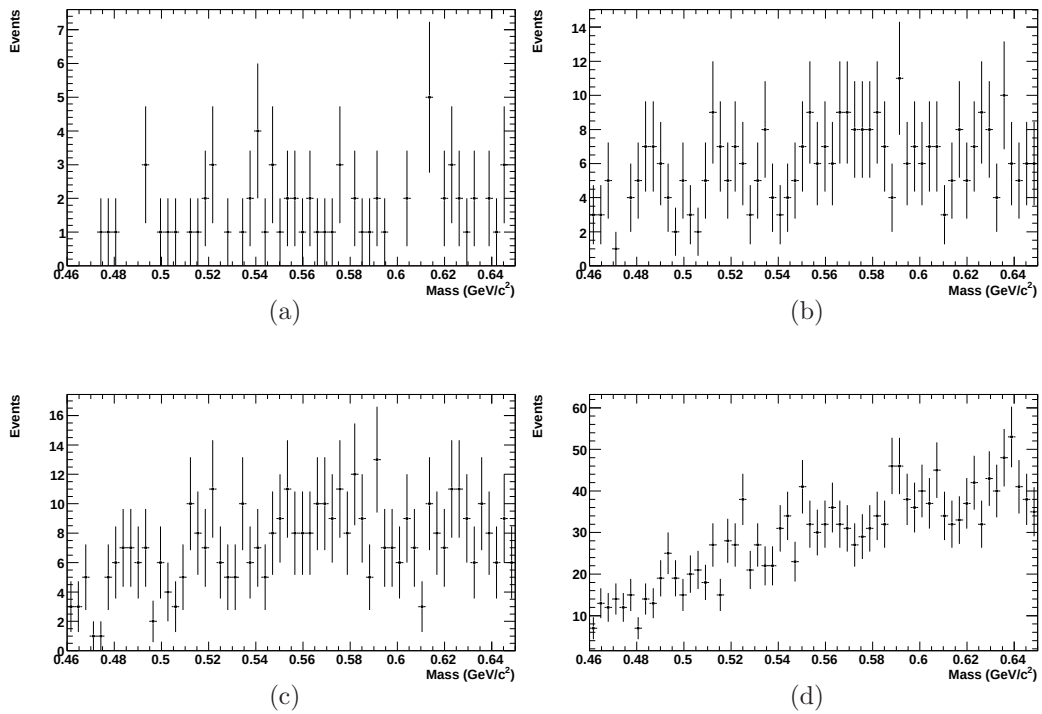

Figure C.1: All contributing background in the η fit region (separated by type). No scaling. (a) uds, (b) $c\bar{c}$, (c) $q\bar{q}$, (d) τ

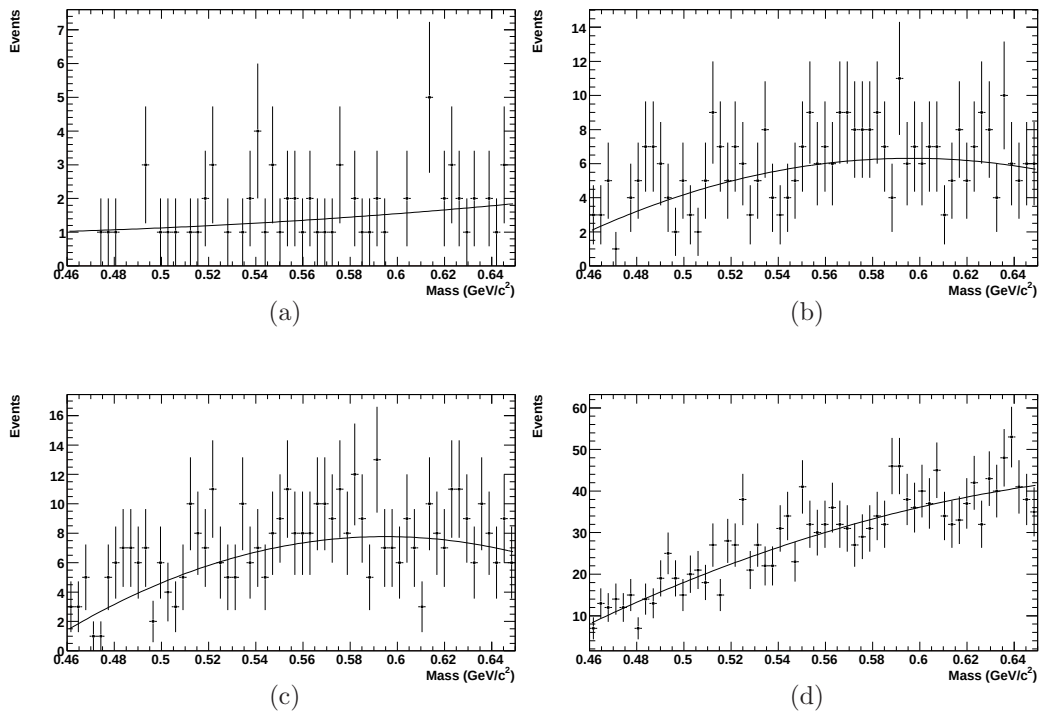

Figure C.2: All contributing background in the η fit region (separated by type). Each is fit does not use data points found between 520-570 MeV/c^2 to determine the parameters for the background fit. (a) *uds* (b) $c\bar{c}$ (c) $q\bar{q}$ (d) τ.

C.2 $N_{q\bar{q}+\tau}$ Background Contamination

To verify our background contamination estimate of η from either generic τ or $q\bar{q}$ events, we investigate a number of small regions of pseudomass above the initial cut of $m_\tau < 1.8\,\mathrm{GeV}/c^2$. Since there is a small tail of signal events just above the $1.8\,\mathrm{GeV}/c^2$, we needed to investigate the following regions: 1.80-2.00 GeV/c^2,1.85-2.05 GeV/c^2, 1.90-2.10 GeV/c^2. The data is plotted in Figure C.3 and the full Monte Carlo is plotted in Figure C.4, there is clearly some evidence for η events above the m_τ cut.

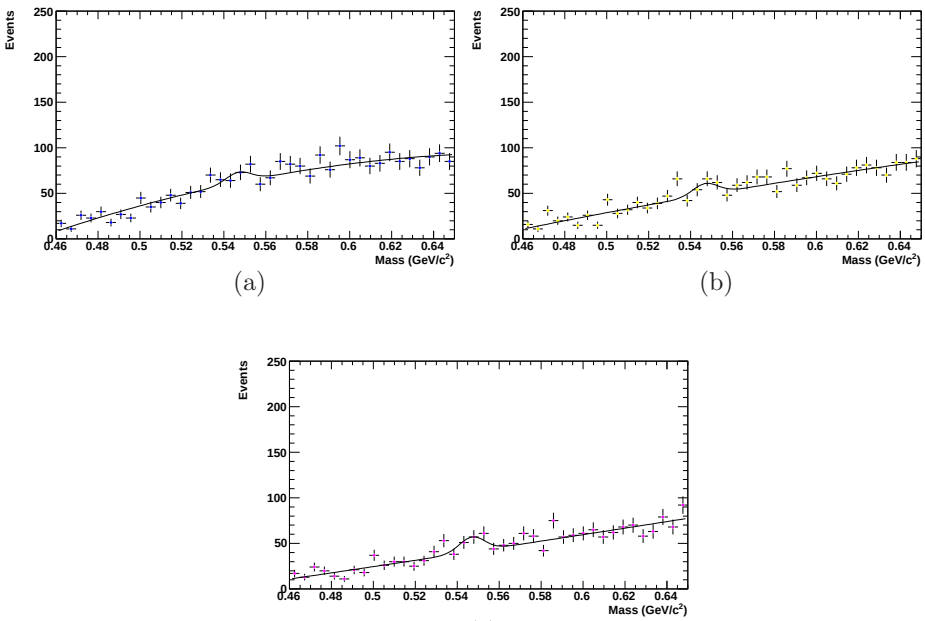

Figure C.3: Plot of the mass of the π^+ π^- π^0 combinations in the signal hemisphere after all selection criteria have been applied except the pseudomass requirement; Each plot imposes a different constraint on the mass of the τ lepton in the signal hemisphere: (a) 1.80-2.00 GeV/c^2 (b) 1.85-2.05 GeV/c^2 (c) 1.90-2.10 GeV/c^2. (Data)

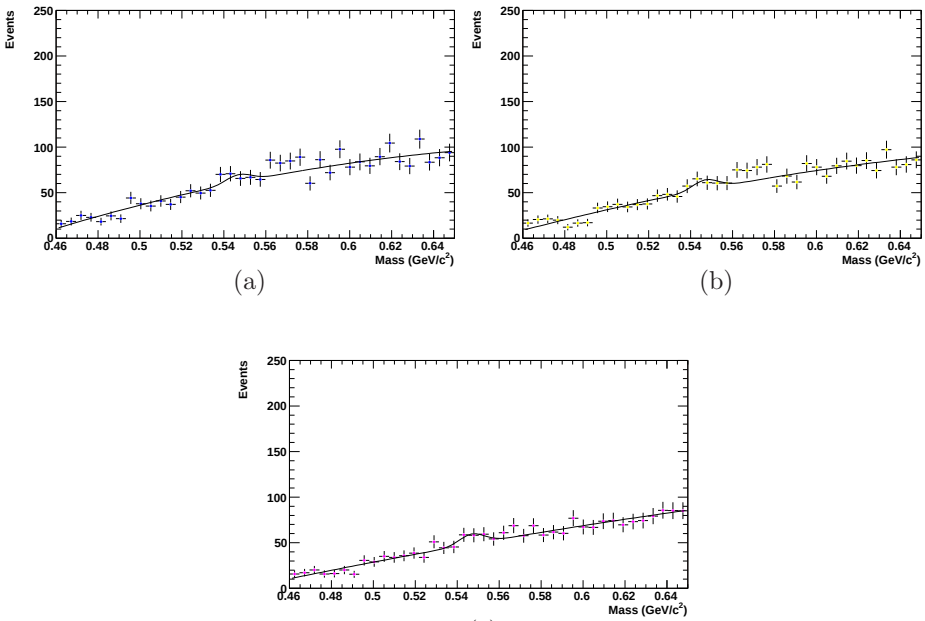

Figure C.4: Plot of the mass of the π^+ π^- π^0 combinations in the signal hemisphere after all selection criteria have been applied except the pseudomass requirement; Each plot imposes a different constraint on the mass of the τ lepton in the signal hemisphere: (a) 1.80-2.00 GeV/c^2 (b) 1.85-2.05 GeV/c^2 (c) 1.90-2.10 GeV/c^2. (All Monte Carlo Samples, including Signal Monte Carlo)

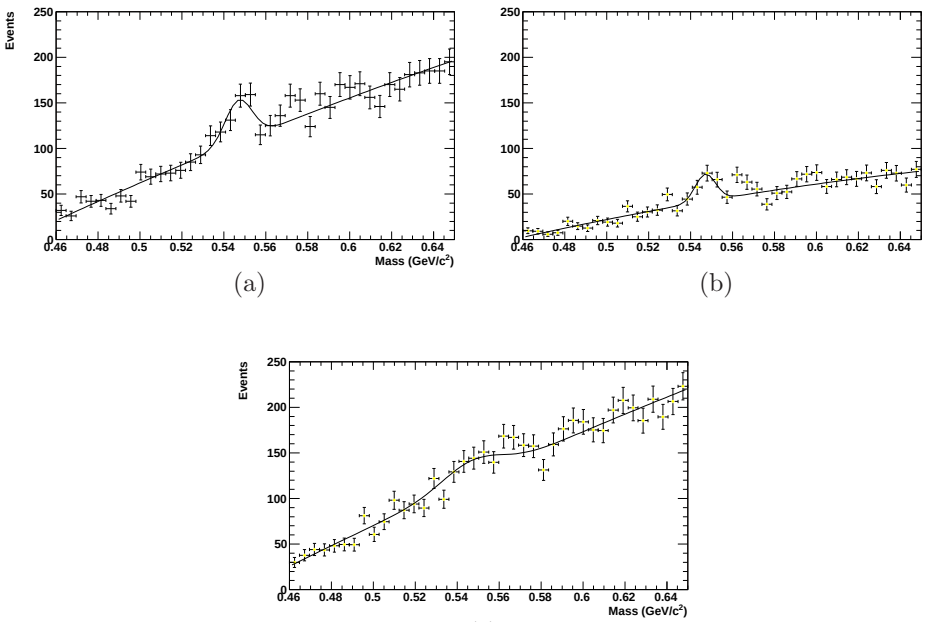

Figure C.5: Plot of the mass of the $\pi^+ \pi^- \pi^0$ combinations in the signal hemisphere after all selection criteria except the pseudomass requirement; The additional requirement that the pseudomass of the τ in the signal hemisphere must be greater than $1.8\,\mathrm{GeV}/c^2$ has been applied. All plots have been fitted with a quadratic function to describe the combinatorial background and a Gaussian with a mean fixed to $0.547\,\mathrm{GeV}/c^2$. (a) is data; (b) is $q\bar{q}$ and (c) is entire Monte Carlo sample.

To determine the number of η's in each of the pseudomass bins, we fit each histogram with Gaussian with a fixed mean (the mean is 0.547 GeV/c^2) and a fixed width (the width is 6 MeV/c^2)[1]. The number of data events with η mesons between 1.80-2.00 GeV/c^2 and 1.85-2.05 GeV/c^2 pseudomass bins are consistent with Monte Carlo. When considering the pseudomass range of 1.90-2.10 GeV/c^2 there is a small discrepancy (on the order of 15 events) between the number of η's found in data than in Monte Carlo.

However if we consider all events with pseudomass greater than 1.8 GeV/c^2, and fit the π^+ π^- π^0 mass spectrum using a free Gaussian resolution parameter but a fixed mean (the mean is fixed to 0.547 GeV/c^2), we find that there are double the number of η candidates when comparing only the $q\bar{q}$ Monte Carlo sample to data (see Figure C.5)[2].

We attribute this discrepancy in the number of η mesons near the τ mass and line shape of the η resonance to incorrect modelling of τ, UDS and $c\bar{c}$ events at energies near the τ pair-production threshold, and assign a 2.2%[3] systematic error on the number of η mesons that might be associated with background instead of true signal events.

[1] see §5.1

[2] The widths of both these peaks are on the order of 5 MeV/c^2. The number of η's observed above the τ mass for data is 155 ± 41 and $q\bar{q}$ Monte Carlo is 76 ± 40. However, when considers the entire Monte Carlo sample, the number of observed η mesons in between the entire Monte Carlo sample is consistent with the number found in data. However the width of η peak associated with the entire Monte Carlo sample is much larger than data.

[3] (2%$\approx$ 15/661)

Appendix D

D.1 Meson Classification [1]

Mesons are the only hadrons with zero baryon number. In the standard quark model, mesons are quark-antiquark($q_1\bar{q}_2$) bound states. If the orbital angular momentum of the state is L, then the parity P is $(-1)^{L+1}$. Meson spin, S, is either 0 or 1, so total angular momentum of the meson J is restricted to between $\max(0, |L-S|) \leq J \leq |L+S|$. Charge conjugation parity, or C-parity, eigenvalues are given by $C = (-1)^{L+S}$. Few mesons are eigenstates of charge conjugation parity, thus classification is limited to states composed of quark-antiquark pairs ($q_1\bar{q}_1$). The concept of charge conjugation is used in the definition of G-parity ($G = (-1)^{L+S+I}$) and mesons are classified in J^{PC} multiplets.

Names are assigned to those states with quantum numbers compatible with being $q_1\bar{q}_2$ states. The rows of the table (D.1) and (D.2) show the possible quark content. The columns give the possible parity/charge conjugation states,

$$PC = -+, +-, --, ++ \tag{D.1}$$

these combinations correspond with the angular momentum states ${}^{2S+1}L_J$ of the system being

$${}^{2S+1}L_J = {}^1(L \text{ even})_J, {}^1(L \text{ odd})_J, {}^3(L \text{ even})_J, {}^3(L \text{ odd})_J, \tag{D.2}$$

Here J, L, and S are the total, orbital, and spin angular momenta of the $q_1\overline{q_2}$ system.

The quantum numbers are related by

$$P = (-1)^{L+1}, C = (-1)^{L+S}, \text{ and } G = (-1)^{L+S+1}. \tag{D.3}$$

$q\bar{q}$ content	0^{-+}	0^{++}
$u\bar{d}$,$d\bar{u}$,$u\bar{u} - d\bar{d}$ (I=1)	π	a
$u\bar{u} - d\bar{d}$ and/or $s\bar{s}$ (I=0)	η, η'	f, f'

Table D.1: Symbols for scalar and pseudoscalar mesons with strangeness and heavy-flavour quantum numbers equal to zero.

$q\bar{q}$ content	1^{+-}	1^{--}
$u\bar{d}$,$d\bar{u}$,$u\bar{u} - d\bar{d}$ (I=1)	b	ρ
$u\bar{u} - d\bar{d}$ and/or $s\bar{s}$ (I=0)	h, h'	ω, ϕ

Table D.2: Symbols for axial vector and vector mesons with strangeness and heavy-flavour quantum numbers equal to zero.